Detecting Sunyaev–Zel'dovich clusters with *Planck* – II. Foreground components and optimized filtering schemes

B. M. Schäfer,[1]* C. Pfrommer,[1]* R. M. Hell[1]* and M. Bartelmann[2]*

[1]*Max-Planck-Institut für Astrophysik, Karl-Schwarzschild-Straße 1, Postfach 1317, 85741 Garching, Germany*
[2]*Institut für theoretische Astrophysik, Universität Heidelberg, Albert-Ueberle-Straße 2, 69120 Heidelberg, Germany*

ABSTRACT

The *Planck* mission is the most sensitive all-sky cosmic microwave background (CMB) experiment currently planned. The High-Frequency Instrument (HFI) will be especially suited for observing clusters of galaxies by their thermal Sunyaev–Zel'dovich (SZ) effect. In order to assess *Planck*'s SZ capabilities in the presence of spurious signals, a simulation is presented that combines maps of the thermal and kinetic SZ effects with a realization of the CMB, in addition to Galactic foregrounds (synchrotron emission, free–free emission, thermal emission from dust, CO-line radiation) as well as the submillimetric emission from celestial bodies of our Solar system. Additionally, observational issues such as the finite angular resolution and spatially non-uniform instrumental noise of *Planck*'s sky maps are taken into account, yielding a set of all-sky flux maps, the autocorrelation and cross-correlation properties of which are examined in detail. In the second part of the paper, filtering schemes based on scale-adaptive and matched filtering are extended to spherical data sets, that enable the amplification of the weak SZ signal in the presence of all contaminations stated above. The theory of scale-adaptive and matched filtering in the framework of spherical maps is developed, the resulting filter kernel shapes are discussed and their functionality is verified.

Key words: methods: numerical – galaxies: clusters: general – cosmic microwave background.

1 INTRODUCTION

The Sunyaev–Zel'dovich (SZ) effect (Sunyaev & Zel'dovich 1972, 1980; Birkinshaw 1999; Rephaeli 1995) is the most important extragalactic source of secondary anisotropies in the cosmic microwave background (CMB) sky. The thermal SZ effect is explained by the fact that CMB photons are put in thermal contact with electrons of the hot intracluster medium (ICM) by Compton interactions which causes a transfer of energy from the ICM to the CMB. Because of the smallness of the Thompson cross-section and of the diluteness of the ICM this transfer of thermal energy is small. In the direction of a cluster, low-energetic photons with frequencies below $\nu = 217\,\text{GHz}$ are removed from the line of sight. At frequencies above $\nu = 217\,\text{GHz}$ CMB photons are scattered into the line of sight, causing a distinct modulation of the CMB surface brightness as a function of observing frequency, which enables the detection of clusters of galaxies in microwave data.

In contrast, in the kinetic effect it is the peculiar motion of a cluster along the line of sight relative to the CMB frame that induces CMB surface brightness fluctuations. The peculiar motion of the cluster causes the CMB to be anisotropic in the cluster frame. Due to this symmetry breaking of the scattering geometry, photons scattered into the line of sight are shifted in frequency, namely to higher frequencies, if the cluster is moving towards the observer.

The *Planck* mission will be especially suited to detect SZ clusters due to its sensitivity, its spectroscopic capabilities, sky coverage and spatial resolution. It is expected to yield a cluster catalogue containing $\simeq 10^4$ entries. The detection of SZ clusters is the topic of many interesting papers (cf. Barbosa et al. 1996; Aghanim et al. 1997; Hobson et al. 1998; Barbosa, Bartlett & Blanchard 2000; Cayón et al. 2000; Diego et al. 2002; Herranz et al. 2002a; Stolyarov et al. 2002; White 2003; Geisbüsch, Kneissl & Hobson 2005), where the detectability of SZ clusters is discussed with special emphasis on the signal amplification and extraction and the estimation of cosmological parameters.

In this work we aim at modelling the astrophysical and instrumental aspect connected to the observation of SZ clusters to high accuracy: a simulation is presented that combines all-sky maps of both SZ effects with a realization of the CMB, with four different

*E-mail: spirou@mpa-garching.mpg.de (BMS); pfrommer@mpa-garching.mpg.de (CP); reinhard@mpa-garching.mpg.de (RMH); mbartelmann@ita.uni-heidelberg.de (MB)

Galactic foreground components (thermal dust, free–free emission, synchrotron emission and emission from rotational transitions of CO molecules) and with maps containing the submillimetric emission from planets and asteroids of the Solar system. *Planck*'s frequency response, beam shapes and noise properties are modelled conforming to the present knowledge of *Planck*'s receivers, its optical system and scanning strategy. For amplifying and extracting the weak SZ signal in the presence of overwhelming backgrounds, filter kernels based on matched and scale-adaptive filtering pioneered by Herranz et al. (2002b) are derived and discussed in detail.

In this paper, we intend to improve the simulations referred to above by constructing realistic SZ maps, by adding two new foregrounds (rotational transitions of carbon monoxide (CO) and thermal emission from planets and asteroids), by changing the emission law describing the synchrotron emission to comply with new results from *Wilkinson Microwave Anisotropy Probe* (*WMAP*), by employing simulated scan paths for the spatially non-uniform noise characteristics of *Planck* and by convolving the sky emission components with realistic frequency response functions. Key results are the autocorrelation and cross-correlation properties of the sky maps recorded in *Planck*'s frequency bands and the filter kernel shapes designed for separating the weak SZ signal.

The filtering scheme that we build on is the powerful concept of matched and scale-adaptive filtering formulated by Sanz, Herranz & Martínez-Gónzalez (2001) as a functional extremization problem and generalized to multifrequency observations by Herranz et al. (2002b). In this paper, matched and scale-adaptive filtering is extended to perform all calculations in spherical coordinates and to use spherical harmonical transforms for the analysis of fluctuation amplitudes as a function of angular scale. Filtering methods do not require prior approximate knowledge of the power spectra of the emission components and offer the advantage of relative computational simplicity in comparison to component separation methods (e.g. the harmonic space maximum-entropy method proposed by Stolyarov et al. 2002), which are computationally demanding. Applying this specific method, Geisbüsch et al. (2005) have recovered 10^4 clusters in a simulation comparable to ours and found that the component separation method is very effective in suppressing the Galactic foregrounds.

The paper is structured as follows. After a brief recapitulation of the SZ effect in Section 2, the *Planck* satellite and instrumental issues connected to the observation of CMB anisotropies are described in Section 3. The foreground emission components are introduced in Section 4. The steps in the simulation of flux maps for the various *Planck* channels are described and their correlation properties are examined in Section 5. The theory of matched and scale-adaptive filtering is extended to spherical data sets and the resulting filter kernel shapes are in detail discussed in Section 6. A summary in Section 7 concludes the paper.

Throughout the paper, the cosmological model assumed is the standard Lambda cold dark matter (ΛCDM) cosmology, which has recently been supported by observations of the *WMAP* satellite (Spergel et al. 2003). Parameter values have been chosen as $\Omega_M = 0.3, \Omega_\Lambda = 0.7, H_0 = 100\,h\,\mathrm{km\,s^{-1}\,Mpc^{-1}}$ with $h = 0.7, \Omega_B = 0.04, n_s = 1$ and $\sigma_8 = 0.9$.

2 SUNYAEV–ZEL'DOVICH DEFINITIONS

The SZ effects are the most important extragalactic sources of secondary anisotropies in the CMB. Inverse Compton scattering of CMB photons with electrons of the ionized ICM gives rise to these effects and induce surface brightness fluctuations of the CMB sky,

either because of the thermal motion of the ICM electrons (thermal SZ effect) or because of the bulk motion of the cluster itself relative to the comoving CMB frame along the line of sight (kinetic SZ effect).

The relative change $\Delta T/T$ in thermodynamic CMB temperature at position θ as a function of dimensionless frequency $x = h\nu/(k_B\,T_{CMB})$ due to the thermal SZ effect is given by

$$\frac{\Delta T}{T}(\boldsymbol{\theta}) = y(\boldsymbol{\theta})\left(x\frac{e^x+1}{e^x-1} - 4\right) \text{ with} \tag{1}$$

$$y(\boldsymbol{\theta}) = \frac{\sigma_T k_B}{m_e c^2}\int dl\, n_e(\boldsymbol{\theta}, l)T_e(\boldsymbol{\theta}, l), \tag{2}$$

where the amplitude y of the thermal SZ effect is commonly known as the thermal Comptonization parameter, that itself is defined as the line-of-sight integral of the temperature weighted thermal electron density. m_e, c, k_B and σ_T denote electron mass, speed of light, Boltzmann constant and the Thompson cross-section, respectively. The kinetic SZ effect arises due to the motion of the cluster parallel to the line of sight relative to the CMB frame:

$$\frac{\Delta T}{T}(\boldsymbol{\theta}) = -w(\boldsymbol{\theta}) \text{ with } w(\boldsymbol{\theta}) = \frac{\sigma_T}{c}\int dl\, n_e(\boldsymbol{\theta}, l)\upsilon_r(\boldsymbol{\theta}, l). \tag{3}$$

Here, υ_r is the radial component of the cluster velocity. The convention is such that $\upsilon_r < 0$, if the cluster is moving towards the observer. In this case, the CMB temperature is increased. In analogy, the quantity w is referred to as the kinetic Comptonization. The SZ observables are the line-of-sight Comptonizations integrated over the solid angle subtended by the cluster. The quantities $\mathcal{Y}$ and $\mathcal{W}$ are referred to as the integrated thermal and kinetic Comptonizations, respectively:

$$\mathcal{Y} = \int d\Omega\, y(\boldsymbol{\theta}) = d_A^{-2}(z)\frac{\sigma_T k_B}{m_e c^2}\int dV\, n_e T_e, \tag{4}$$

$$\mathcal{W} = \int d\Omega\, w(\boldsymbol{\theta}) = d_A^{-2}(z)\frac{\sigma_T}{c}\int dV\, n_e\upsilon_r. \tag{5}$$

Here, $d_A(z)$ denotes the angular diameter distance of a cluster situated at redshift z.

3 SUBMILLIMETRIC OBSERVATIONS WITH *PLANCK*

The *Planck* mission[1] will perform a polarization sensitive survey of the complete microwave sky in nine observing frequencies from the Lagrange point L_2 in the Sun–Earth system.[2] It will observe at angular resolutions of up to 5.0 arcmin in the best channels and will achieve micro-Kelvin sensitivity relying on bolometric receivers (High-Frequency Instrument, HFI, described in Lamarre, Puget & Bouchet 2003) and on high electron mobility transistors (Low-Frequency Instrument, LFI, see Bersanelli & Mandolesi 2000; Villa et al. 2003). The main characteristics are summarized in Table 1. *Planck*'s beam characteristics are given Section 3.1 and the scanning strategy and the simulation of spatially non-uniform detector noise is outlined in Section 3.2.

---

[1] http://planck.mpa-garching.mpg.de/
[2] http://astro.estec.esa.nl/Planck/

Table 1. Characteristics of *Planck*'s LFI receivers (columns 1–3) and HFI bolometers (columns 4–9): centre frequency ν_0, frequency window $\Delta\nu$ as defined in equations (27) and (28), angular resolution $\Delta\theta$ stated in FWHM, effective noise level σ_N, fluxes $\langle S_{\mathcal{Y}}\rangle$ and $\langle S_{\mathcal{W}}\rangle$ generated by the respective Comptonization of $\mathcal{Y} = \mathcal{W} = 1$ arcmin^2 and the corresponding changes in antenna temperature $\Delta T_{\mathcal{Y}}$ and $\Delta T_{\mathcal{W}}$. Due to *Planck*'s symmetric frequency response window, the thermal SZ effect does not vanish entirely at $\nu = 217$ GHz.

Planck channel	1	2	3	4	5	6	7	8	9
Centre frequency ν_0	30 GHz	44 GHz	70 GHz	100 GHz	143 GHz	217 GHz	353 GHz	545 GHz	857 GHz
Frequency window $\Delta\nu$	3.0 GHz	4.4 GHz	7.0 GHz	16.7 GHz	23.8 GHz	36.2 GHz	58.8 GHz	90.7 GHz	142.8 GHz
Resolution $\Delta\theta$ (FWHM)	33.4 arcmin	26.8 arcmin	13.1 arcmin	9.2 arcmin	7.1 arcmin	5.0 arcmin	5.0 arcmin	5.0 arcmin	5.0 arcmin
Noise level σ_N	1.01 mK	0.49 mK	0.29 mK	5.67 mK	4.89 mK	6.05 mK	6.80 mK	3.08 mK	4.49 mK
Thermal SZ flux $\langle S_{\mathcal{Y}}\rangle$	-12.2 Jy	-24.8 Jy	-53.6 Jy	-82.1 Jy	-88.8 Jy	-0.7 Jy	146.0 Jy	76.8 Jy	5.4 Jy
Kinetic SZ flux $\langle S_{\mathcal{W}}\rangle$	6.2 Jy	13.1 Jy	30.6 Jy	55.0 Jy	86.9 Jy	110.0 Jy	69.1 Jy	15.0 Jy	0.5 Jy
Antenna temperature $\Delta T_{\mathcal{Y}}$	-440 nK	-417 nK	-356 nK	-267 nK	-141 nK	-0.5 nK	38 nK	8.4 nK	0.2 nK
Antenna temperature $\Delta T_{\mathcal{W}}$	226 nK	220 nK	204 nK	179 nK	138 nK	76 nK	18 nK	1.6 nK	0.02 nK

3.1 Beam shapes

The beam shapes of *Planck* are well described by azimuthally symmetric Gaussians $b(\theta) = (1/2\pi\sigma_\theta^2)\exp(-\theta^2/2\sigma_\theta^2)$ with $\sigma_\theta = \Delta\theta/\sqrt{8\ln 2}$. The residuals from the ideal Gaussian shape (ellipticity, higher-order distortions, diffraction rings, far-side lobes, pick-up of stray light) are expected not to exceed the percentage level and are neglected for the purpose of this work. Table 1 gives the angular resolution $\Delta\theta$ in terms of full width at half-maximum (FWHM) of each *Planck* channel for reference.

3.2 Scanning strategy and noise-equivalent maps

CMB observations by *Planck* will proceed in great circles fixed on the ecliptic poles. A single scan will start at the North ecliptic pole, will follow a meridian to the South ecliptic pole and back to the North ecliptic pole by following the antipodal meridian. Such a scan will last one minute and will be repeated sixty times. After that, the rotation axis will be shifted in a precessional motion for 2.5 arcmin (approximately half a beam diameter) and the scan repeated. In this way, the entire sky is mapped once in 180 d.

Fourier transform of the noise time-series of *Planck*'s receivers yields a noise power spectrum $P(f)$ of the shape

$$P(f) = \sigma_N^2 \left[1 + \left(\frac{f}{f_{\text{knee}}}\right)^{-\alpha} \right], \tag{6}$$

that is, the noise consists of two components: a power-law component in frequency f, described by the spectral index α that assuming values $0 \leqslant \alpha \leqslant 2$ and a white noise component, smoothly joined at the frequency f_{knee}.

The $f^{-\alpha}$ part of the noise spectrum originates from zero-point drifts of the detector gain on large time-scales. This power-law component exhibits low-frequency variations that lead to the typical stripe pattern in simulated *Planck* maps due to the scanning strategy (Maino et al. 1999). Algorithms for destriping the maps are a current research topic (e.g. the Mirage algorithm proposed by Yvon & Mayet (2005), MAPCUMBA by Doré et al. (2001) and the max-likelihood algorithm by Natoli et al. (2001)), but it can be expected that the destriping can be done very efficiently such that the remaining noise largely consists of uncorrelated pixel noise.

In order to incorporate uncorrelated pixel noise into the simulation, a set of maps has been constructed, where at each pixel a number from a Gaussian distribution with width σ_N has been drawn. For *Planck*'s HFI receivers, the rms fluctuations σ_N in antenna temperature can be calculated from the noise equivalent power (NEP) and

the sampling frequency $\nu_{\text{sampling}} = 200$ Hz via

$$\sigma_N = \frac{2\,\text{NEP}\sqrt{\nu_{\text{sampling}}}}{k_B\Delta\nu} \quad \text{(HFI)}. \tag{7}$$

Alternatively, for *Planck*'s LFI receivers, the rms fluctuations σ_N in antenna temperature are given by

$$\sigma_N = \sqrt{2}\frac{T_{\text{noise}} + T_{\text{CMB}}}{\sqrt{\Delta\nu/\nu_{\text{sampling}}}} \quad \text{(LFI)}. \tag{8}$$

Values for T_{noise} and NEP can be obtained from *Planck*'s simulation pipeline manual. The resulting effective noise level for all *Planck* channels for a single observation of a pixel is given in Table 1. Formulae and respective parameters are taken from the *Planck* simulation manual, available via *Planck*'s website.

The rms fluctuations σ_N in antenna temperature have to be scaled by $\sqrt{n_{\text{det}}}$ (assuming Poissonian statistics), where n_{det} denotes the number of redundant receivers per channel, because they provide independent surveys of the microwave sky.

From simulated scanning paths it is possible to derive an exposure map using the simmission and multimod utilities. An example of such an exposure map in the vicinity of the North ecliptic pole is given in Fig. 1. Using the number of observations n_{obs} per pixel, it is possible to scale down the noise amplitudes by $\sqrt{n_{\text{obs}}}$ and to obtain a realistic noise map for each channel. Here, we apply the simplification that all detectors of a given channel are arranged collinearly. In this case, the exposure maps will have sharp transitions from well-observed regions around the ecliptic poles to the region around the ecliptic equator. In real observations these transitions will be smoothed out due slight displacements of the optical axes among each other which causes the effective exposure pattern to be a superposition of rotated and distorted single-receiver exposure patterns.

4 FOREGROUND EMISSION COMPONENTS

The observation of the CMB and of SZ clusters is seriously impeded by various Galactic foregrounds and by the thermal emission of celestial bodies of our Solar system. In order to describe these emission components, template maps from microwave surveys are used. Bouchet & Gispert (1999) give a comprehensive review for the foreground components relevant for the *Planck* mission. As foreground components we include thermal emission from dust in the Galactic plane (Section 4.1), Galactic synchrotron (Section 4.2) and free–free emission (Section 4.3), line emission from rotational
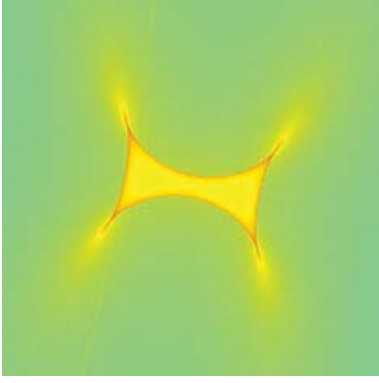
Figure 1. Exposure map (side length $\simeq 70°$) of a single $\nu = 353$ GHz receiver at the North ecliptic pole in logarithmic shading. The displacement of the receivers with respect to the optical axis along with the deliberate oscillation of the *Planck*'s spin axis above and below the ecliptic plane causes the observational rings not to overlap exactly at the poles, but gives rise to the lozenge-shaped pattern in the sky-coverage map. On average, the pixels inside the lozenge are observed roughly 100 times, compared to $\sim$20 times outside. Pixels on the edges of the lozenge are observed a few thousand times. The best observed pixels are situated on the tips of the lozenge, where values as high as 2×10^4 are attained. The numbers correspond to the planned mission lifetime of 1 yr. The faint diagonal tangential line on the left-hand side is caused by 2008 being a leap year: the mapping of the entire sky would be completed in 365 d, but there is an additional day available.

transitions of CO molecules in giant molecular clouds (GMCs) (Section 4.4), submillimetric emission from planets (Section 4.5) and from minor bodies of the Solar system (Section 4.6). Foreground components omitted at this stage are discussed in Section 4.7.

In this work, no attempt is made at modelling the interactions between various foreground components because of poorly known parameters such as the spatial arrangement along the line of sight of the emitting and absorbing components. Exemplarily, the reader is referred to Finkbeiner (2003), where the absorption of Galactic free–free emission by dust is discussed.

4.1 Galactic dust emission

At frequencies above $\sim$100 GHz, the thermal emission from dust in the disc of the Milky Way is the most prominent feature in the microwave sky. Considerable effort has been undertaken to model the thermal emission from Galactic dust (Schlegel, Finkbeiner & Davis 1997, 1998; Finkbeiner, Davis & Schlegel 1999, 2000). The thermal dust emission is restricted to low Galactic latitudes and the thin disc is easily discernible.

The input template map (see Fig. 2) is derived from an observation at a wavelength of $\lambda = 100\,\mu$m, i.e. $\nu_0 = 3$ THz. Its amplitudes A_{dust} are given in MJy sr^{-1}, which are extrapolated to the actual frequency channels of *Planck* using a two-component model suggested by C. Baccigalupi (personal communication). Despite the fact that the dust is expected to spread over a large range of temperatures, the model reproduces the thermal emission remarkably well. This model yields for the flux $S_{\text{dust}}(\nu)$:

$$S_{\text{dust}}(\nu) = \frac{f_1 q \, (\nu/\nu_0)^{\alpha_1} \, B(\nu, T_1) + f_2 \, (\nu/\nu_0)^{\alpha_2} \, B(\nu, T_2)}{f_1 q \, B(\nu_0, T_1) + f_2 B(\nu_0, T_2)} \, A_{\text{dust}}. \quad (9)$$

The choice of parameters used is: $f_1 = 0.0363$, $f_2 = 1 - f_1$, $\alpha_1 = 1.67$, $\alpha_2 = 2.70$, $q = 13.0$. The two dust temperatures are $T_1 = 9.4$ K and $T_2 = 16.2$ K. The function $B(\nu, T)$ denotes the Planckian
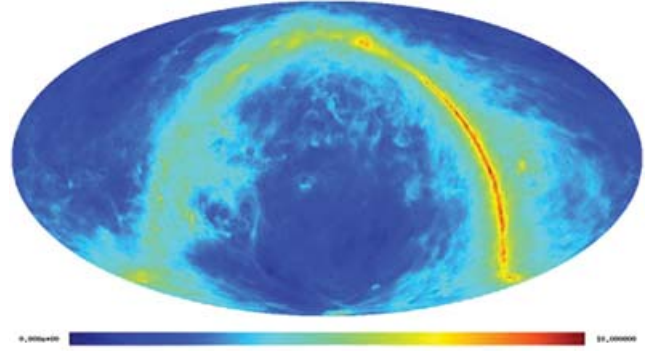
Figure 2. Sky map of the antenna temperature increase caused by dust emission in the $\nu = 100$ GHz channel: the shading is proportional to arsinh $(T_A(\nu = 100\,\text{GHz})\,\mu\text{K}^{-1})$. Ecliptic coordinates have been chosen. This map has been derived from the dust-template map provided by Schlegel et al. (1998).
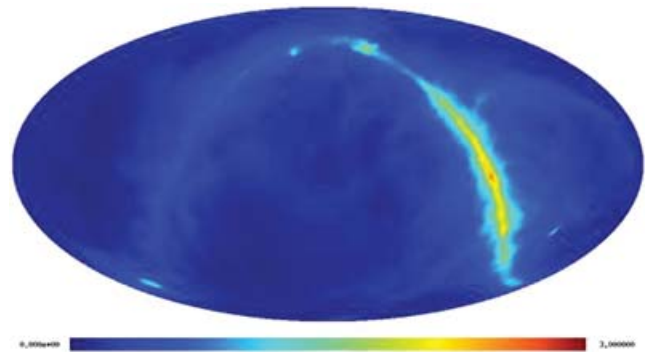
emission law:

$$B(\nu, T) = \frac{2h}{c^2} \frac{\nu^3}{\exp(h\nu/k_B T) - 1}. \quad (10)$$

4.2 Galactic synchrotron emission

Relativistic electrons of the interstellar medium produce synchrotron radiation by spiralling around magnetic field lines, which impedes CMB observations most strongly at frequencies below 100 GHz. The synchrotron emission reaches out to high Galactic latitude and is an important ingredient for modelling foreground emission in microwave observations. An all-sky survey at an observing frequency of 408 MHz has been compiled by Haslam et al. (1981, 1982) and adopted for usage with *Planck* by Giardino et al. (2002) (see Fig. 3). The average angular resolution of this survey is $0°85$ (FWHM).

Recent observations with *WMAP* (Bennett et al. 2003b) indicate that the spectral slope of the synchrotron emission changes dramatically from $\gamma = -0.75$ at frequencies below 22 GHz to $\gamma = -1.25$ above 22 GHz. Theoretically, this may be explained by a momentum-dependent diffusion coefficient for cosmic ray electrons. In order to take account of this spectral steepening, the amplitudes A_{synchro} are multiplied with a prefactor in order to obtain

Figure 3. Sky map of the antenna temperature increase caused by synchrotron emission in the $\nu = 100$ GHz channel in ecliptic coordinates: the shading is proportional to arsinh $(T_A(\nu = 100\,\text{GHz})\,\mu\text{K}^{-1})$. The survey undertaken by Haslam et al. (1982) was used to construct this template.
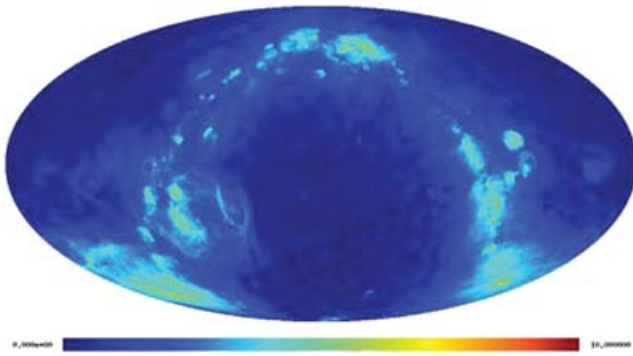
Figure 4. Sky map of the antenna temperature increase caused by free–free emission in the $\nu = 100\,\mathrm{GHz}$ channel: the shading is proportional to arsinh $(T_\mathrm{A}(\nu = 100\,\mathrm{GHz})\,\mu\mathrm{K}^{-1})$. Ecliptic coordinates have been chosen. This map has been derived from the Hα template map provided by Finkbeiner (2003).

Figure 5. Sky map of the increment in antenna temperature due to CO-line emission in the $\nu = 100\,\mathrm{GHz}$ channel in ecliptic coordinates: the shading is proportional to arsinh $(T_\mathrm{A}(\nu = 100\,\mathrm{GHz})\,\mu\mathrm{K}^{-1})$. The maps shows the rotational transition of the CO molecule from the first excited state into the ground state at $\nu_{0\rightarrow1} = 115\,\mathrm{GHz}$ as derived by Dame et al. (2001) for a temperature of $T_\mathrm{CO} = 20\,\mathrm{K}$.

the synchrotron fluxes at $\nu = 22\,\mathrm{GHz}$. This value is then extrapolated to *Planck*'s observing frequencies with a spectral index of $\gamma = -1.25$. The amplitudes A_synchro of the input map are given in units of MJy sr^{-1}, and for the flux $S_\mathrm{synchro}(\nu)$ one thus obtains

$$S_\mathrm{synchro}(\nu) = \sqrt{\frac{22\,\mathrm{GHz}}{408\,\mathrm{MHz}}}\, A_\mathrm{synchro}\left(\frac{\nu}{408\,\mathrm{MHz}}\right)^{-1.25}. \tag{11}$$

Here, the fact that the synchrotron spectral index shows significant variations across the Milky Way due to varying magnetic field strength is ignored. Instead, a spatially constant spectral behaviour is assumed. In contrast, the *Planck* reference sky model Bouchet & Gispert (1999) relies on a spectral index map for doing a spatially varying extrapolation of the synchrotron fluxes to *Planck*'s observing frequencies. In the model, however, the spectral break at $\nu = 22\,\mathrm{GHz}$ observed by *WMAP* discussed above is not implemented, giving rise likely underestimated fluxes, approximately by almost one and a half order of magnitude at $\nu = 100\,\mathrm{GHz}$ (for a spectral index of $\gamma = -1.5$).
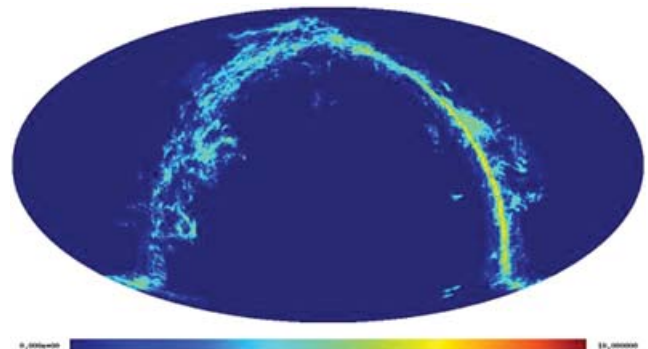
4.3 Galactic free–free emission

The Galactic ionized plasma produces free–free emission, which is an important source of contamination in CMB observations, as recently confirmed by Bennett et al. (2003b) in *WMAP* observations. Aiming at modelling the free–free emission at microwave frequencies, we rely on an Hα template provided by Finkbeiner (2003), which is shown in Fig. 4. Modelling of the free–free emission component on the basis of an Hα template is feasible because both emission processes depend on the emission measure $\int n_\mathrm{e}^2\,\mathrm{d}l$, where n_e is the number density of electrons. This template is a composite of three Hα surveys and is because of its high resolution (on average 6.0 arcmin FWHM) particularly well suited for CMB foreground modelling. The morphology of the free–free map is very complex and the emission reaches out to intermediate Galactic latitude.

For relating Hα fluxes $A_\mathrm{H\alpha}$ given in units of Rayleigh to the free–free signal's antenna temperature $T_\mathrm{free-free}$ measured in K, Valls-Gabaud (1998) gives the formula

$$\frac{T_\mathrm{free-free}\,(\mu\mathrm{K})}{A_\mathrm{H\alpha}(R)} \simeq 14.0 \left(\frac{T_\mathrm{p}}{10^4\,\mathrm{K}}\right)^{0.317} 10^{290\,\mathrm{K}\,T_\mathrm{p}^{-1}}\, g_\mathrm{ff}\left(\frac{\nu}{10\mathrm{GHz}}\right)^{-2}. \tag{12}$$

T_p denotes the plasma temperature and is set to $10^4\,\mathrm{K}$ in this work. An approximation for the Gaunt factor g_ff valid for microwave frequencies in the range $\nu_\mathrm{p} \ll \nu \ll k_\mathrm{B}T/h$ (ν_p is the plasma frequency) is given by Finkbeiner (2003)

$$g_\mathrm{ff} = \frac{\sqrt{3}}{\pi}\left\{\ln\left[\frac{(2k_\mathrm{B}T_\mathrm{p})^{3/2}}{\pi e^2 \nu\sqrt{m_\mathrm{e}}}\right] - \frac{5}{2}\gamma_\mathrm{E}\right\}, \tag{13}$$

where e and m_e denote electron charge and mass (in Gaussian units) and $\gamma_\mathrm{E} \simeq 0.57721$ is Euler's constant. The contribution of fractionally ionized helium to the free–free emissivity as well as the absorption by interstellar dust has been ignored because of its being only a small contribution in the first case and because of poorly known parameters in the latter case. The antenna temperature can be converted to the free–free flux $S_\mathrm{free-free}(\nu)$ by means of

$$S_\mathrm{free-free}(\nu) = 2\frac{\nu^2}{c^2}\, k_\mathrm{B}T_\mathrm{free-free}\ (\mathrm{K}). \tag{14}$$

Concerning the free–free emission, there might be the possibility of an additional free–free component uncorrelated with the Hα emission. This hot gas, however, should emit X-ray line radiation, which has not been observed. Comparing this free–free model to *Planck*'s reference sky model, one should mention that although both models only calculate the emission from optically thin plasma, they use extrapolation formulae with different frequency dependence and slightly different approximations to the Gaunt factor. While the values of the Gaunt factors agree within a few per cent, the extrapolation formulae give differ by a factor of a few over *Planck*'s frequency range, yielding smaller values for Valls-Gabaud (1998) compared to Dickinson, Davies & Davis (2003), indicating the uncertainty in the amplitude of the free–free emission component. The smaller value of $T_\mathrm{p} = 7000\,\mathrm{K}$ for the plasma temperature advocated by Dickinson et al. (2003) would yield a free–free flux smaller by 25 per cent for typical *Planck* frequencies of a few hundred GHz.

4.4 CO-lines from giant molecular clouds

In a spiral galaxy such as the Milky Way, a large fraction of the interstellar medium is composed of molecular hydrogen, that resides in GMCs, objects with masses of 10^4–$10^6\,\mathrm{M}_\odot$ and sizes of 50–200 pc. Apart from molecular hydrogen, the GMCs contain CO molecules in significant abundance. The rotational transitions of the CO molecule at 115 GHz and higher harmonics thereof constitute a

source of contamination for all *Planck* HFI channels. An extensive search for atomic and molecular transition lines was undertaken by Bennett et al. (1994) with the FIRAS instrument onboard *COBE*.

The CO contamination is modelled by employing a mosaic of CO surveys assembled by Dame, Hartmann & Thaddeus (1996, 2001) into the all-sky map depicted in Fig. 5. It shows the velocity-integrated intensity of the transition from the first excited state ($J = 1$) to the ground state ($J = 0$) close to the Galactic plane ($b < 5°$), and additionally comprises a few CO clouds at higher Galactic latitude, as well as the Large Magellanic Cloud and the Andromeda galaxy M 31. Due to the composition of the map, the angular resolution is not uniform, but the best resolution of $\simeq 7.5$ arcmin is reached for a large area around the Galactic plane.

From this map, it is possible to derive the line intensities of the higher harmonics, assuming thermal equilibrium. The frequency ν for a transition from a state of rotational quantum number J to a state with quantum number $J + 1$ follows from elementary quantum mechanics. The rotational energy of a CO molecule with moment of inertia θ and angular momentum $\boldsymbol{J}$ is $E_{\rm rot} = \boldsymbol{J}^2/2\theta = \hbar^2 J(J+1)/2\theta$. In the last step the quantum number J was introduced. For the transition energy between two subsequent rotation levels, one obtains

$$\nu_{J\leftrightarrow J+1} = 2Qc\,(J+1) = 115\,{\rm GHz}\,(J+1), \tag{15}$$

where $Q = h/8\pi^2 c\theta$ is a measure of the inverse moment of inertia of the molecule and c denotes the speed of light. Thus, the spectrum consists of equidistant lines. The relative intensities of those lines is given by the ratio of their occupation numbers χ_J:

$$\chi_J = (2J+1)\exp\left[-\frac{Qhc}{k_{\rm B}T_{\rm CO}}J(J+1)\right], \tag{16}$$

that is, the relative line intensities $q_{J\leftrightarrow J+1}$ of two consecutive lines is given by

$$q_{J\leftrightarrow J+1} = \frac{\chi_{J+1}}{\chi_J} = \frac{2J+3}{2J+1}\,\exp\left[-\frac{2Qhc}{k_{\rm B}T_{\rm CO}}\,(J+1)\right]. \tag{17}$$

χ_J is determined by a statistical weight $(2J+1)$ reflecting the degeneracy of angular momentum and a Boltzmann factor. For the determination of line intensities thermal equilibrium is assumed, common estimates for the temperature inside GMCs are $T_{\rm CO} = 10$–30 K. For the purpose of this work, we choose $T_{\rm CO} = 20$ K. From the brightness temperature $T_{\rm A}$ one obtains the CO flux $S_{\rm CO-line}(\nu)$ by means of the following equation:

$$S_{\rm CO-line}(\nu) = 2\frac{\nu^2}{c^2}\,k_{\rm B}T_{\rm A}\,({\rm K})\,p(\nu - \nu_{J\leftrightarrow J+1}), \tag{18}$$

where the line shape $p(\nu - \nu_{J\leftrightarrow J+1})$ is assumed to be small in comparison to *Planck*'s frequency response windows such that its actual shape (e.g. a Voigt profile) is irrelevant.

4.5 Planetary submillimetric emission

Planets produce infrared and submillimetric radiation by absorbing sunlight and by re-emitting this thermal load imposed by the Sun. The investigation of the thermal properties of Mars, Jupiter and Saturn has been the target of several space missions (Griffin et al. 1986; Goldin et al. 1997, to name but a few). For the description of the submillimetric thermal emission properties of planets, an extension to the Wright & Odenwald model (Neugebauer et al. 1971; Wright 1976) was used. The orbital motion of the planets is sufficiently fast such that their movements including their epicyclic motion relative to the Lagrangian point L_2, *Planck*'s observing position, has to be taken into account. All planets are imaged twice in approximate
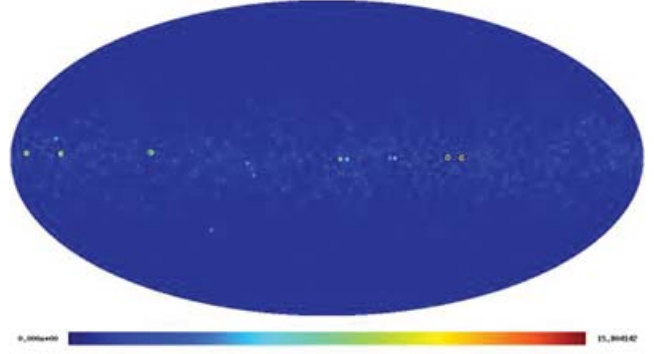
Figure 6. Sky map of increment in antenna temperature $T_{\rm A}$ produced by planets and asteroids in the $\nu = 30$ GHz channel at 33.4 arcmin resolution (FWHM). The colour coding is proportional to arsinh ($T_{\rm A}(\nu = 100\,{\rm GHz})\,{\rm nK}^{-1}$). The asteroids reach ecliptic latitudes of $|\beta| \lesssim 30°$. The pronounced signals are produced by planets, which (due to *Planck*'s scanning strategy) appear twice. The observable planets comprise (from left- to right-hand side) Saturn, Mars, Uranus, Neptune and Jupiter. The epicyclic motion of Mars is sufficiently fast to counteract the parallactic displacement such that it appears only once.

half-year intervals due to *Planck*'s scanning strategy, while showing tiny displacements from the ecliptic plane because of the Lissajous orbit of *Planck* around L_2 and their orbital inclinations.

The heat balance equation for a planet or asteroid reads as

$$E + F + W \equiv P_{\rm emission} = P_{\rm absorption} \equiv I + R, \tag{19}$$

where E denotes the heat loss by thermal emission (i.e. the signal for *Planck*), F the heat flux outward from the interior of the planet, W is the heat lost by conduction to the planet's atmosphere, I is the solar radiation absorbed and R is the heating of the planet caused by the back-scattering of radiation emanating from the surface of the planet by the atmosphere. The definition of these quantities is given by equations (20)–(24):

$$E = \epsilon\,\sigma\,T_{\rm planet}^4, \tag{20}$$

$$F = k\,\frac{\partial T_{\rm planet}}{\partial x}, \tag{21}$$

$$I = \frac{(1-A)G}{r^2}\cos(\theta^*)\cos\left(\frac{2\pi t}{\tau}\right), \tag{22}$$

$$R = \gamma\,\frac{(1-A)G}{r^2}\cos(\theta^*)\cos\left(\frac{2\pi t}{\tau}\right) = \gamma\,I_{\rm max}, \tag{23}$$

and

$$W = \kappa\,F. \tag{24}$$

Here, ϵ is the surface emissivity of the planet, σ is the Stefan–Boltzmann constant, $T_{\rm planet}$ is the planet's temperature, k the coefficient of heat conduction, A the planet's bolometric albedo, G the solar constant (i.e. the energy flux density of solar irradiation at the Earth's mean distance), r the distance of the planet to the Sun in astronomical units, τ the planet's rotation period and θ^* the geographical latitude of the radiation absorbing surface element. The temperature distribution in the interior of the planet at radial position x is controlled by the heat conduction equation:

$$c\,\frac{\partial T_{\rm planet}}{\partial t} = k\,\frac{\partial^2 T_{\rm planet}}{\partial x^2}, \tag{25}$$

with the specific heat per unit volume c.

In our model, the heat loss R of the planet's surface due to conduction to the planet's atmosphere is taken to be a constant fraction of the heat flux F outward from the interior of the planet, the constant of proportionality being κ, for which we assumed $\kappa = 0.1$. Similarly, the heat gain by back-scattering radiation by the atmosphere R was assumed to be a constant fraction γ of the local noon solar flux I_{max}, where γ was taken to be $\gamma = 0.01$. The system of differential equations (20)–(24) dependent on time t and on solar distance r constitutes a heat conduction problem with periodic excitation (by the planet's rotation). Thus, the heat balance of the planets is modelled by periodic solutions of the Laplacian heat conduction differential equations to yield the temperature distribution on the surface of the planet. It was solved iteratively by applying Laplace transforms with periodic boundary conditions. The integration over the planet's surface then yields the radiation flux. In the calculation, we addressed rocky and gaseous planets differently with respect to their thermal properties. Furthermore, the giant gaseous planets are known to have internal sources of heat generation, which also has been taken account of by increasing the incoming heat flux I by a correction factor τ (with the numerical values $\tau_{Jupiter} = 1.7$, $\tau_{Saturn} = 1.8$, $\tau_{Uranus} = 1.1$ and $\tau_{Neptune} = 2.6$ taken from Unsöld & Baschek 2002).

The brightest point source in the microwave sky due to the planetary thermal emission is Jupiter, causing an increase in antenna temperature of $T_{Jupiter} = 93.6$ mK in the $\nu = 100$ GHz channel, followed by Saturn with $T_{Saturn} = 15.0$ mK. All outer planets apart from Pluto will be visible for *Planck*. Estimates show that even Galilean satellites Ganymede, Callisto, Io and Europa and Saturn's moon Titan are above the detection threshold of *Planck*, but as they do not move away from their planets farther than a few arcmin, which is well within *Planck*'s instrumental beam, they are outshone by the stray light from Jupiter and Saturn, respectively, and for that reason not included in our analysis.

Due to the planet's being point sources, their fast movement and their diverse surface temperatures it is not feasible to produce a template and extrapolate the fluxes with a common emission law to *Planck* frequencies. Instead, flux maps have been produced directly for each of the nine *Planck* channels separately taking account of the planetary motion, the solution of the heat balance equation laid down above and the finite beamwidth. The analogous holds for asteroids, which are covered in the next section.

4.6 Submillimetric emission from asteroids

Asteroids and minor bodies of the Solar system are easily observed by infrared satellites such as *ISO* and possibly by submillimetric observatories (Müller & Lagerros 1999; Müller 2001). An estimation by Cremonese et al. (2002) shows that a large number of asteroids (∼400) should yield signals detectable by *Planck*. The orbital motion of all asteroids is fast enough to cause double detections at different positions in the sky separated by half a year due to *Planck*'s scanning strategy. In contrast to planets, asteroids are not well restricted to the ecliptic plane and appear up to ecliptic latitudes of $\beta \lesssim 30°$.

The thermal emission properties of asteroids are well understood (for a comprehensive and detailed review, see Lagerros 1996a,b, 1997, 1998) such that asteroids have been used for calibrating detectors (e.g. the *ISO* mission, cf. Müller & Lagerros 1998, 2002) and for determining beam shapes. The thermal model used for describing the submillimetric emission by asteroids is the same extension of the Wright & Odenwald model as for rocky planets. However, additional features that had to be incorporated was the beamed emission

due to surface roughness. Furthermore, in the system of differential equations (20)–(24) terms W and R were neglected due to the absence of atmospheres in asteroids.

Information about the diameter and albedo was derived using the HG-magnitude system in case of asteroids for which those quantities are unknown, otherwise literature values were taken (from Moore 2000, and IAU's *Minor Planet Centre*[3]). For the description of the rotation period, an empirical relation that expresses the rotation period as a function of mass was used in the cases where the rotation period is unknown. The brightest sources include Ceres ($T_{Ceres} = 19.7$ μK), Pallas ($T_{Pallas} = 7.2$ μK), Vesta ($T_{Vesta} = 6.7$ μK) and Davida ($T_{Davida} = 2.1$ μK). The temperatures stated are antenna temperatures measured in the $\nu = 100$ GHz channel at the brightness maximum.

Typical surface temperatures of asteroids are of the order of 150 K, and therefore, *Planck* is observing their thermal emission in the Rayleigh–Jeans regime. For that reason, the number of detectable asteroids increases with observing frequency. For our sample of 5×10^4 asteroids of the *Minor Planet Centre*'s catalogue, we find a couple of asteroids at $\nu = 30$ GHz, a few tens of asteroids at $\nu = 100$ GHz and up to 100 asteroids in the highest frequency band at $\nu = 857$ GHz which is less than the number predicted by Cremonese et al. (2002), who neither took the observation geometry nor the detector response into account. Approximately 1200 asteroids, however, will have fluxes above half of *Planck*'s single-band detection limit estimated for ideal observation conditions and thus they constitute an abundant population of point sources which increases the noise on small scales.

The prediction of comets is very uncertain for the years 2007–2009: many comets are not detected yet, non-active comets are too faint with few exceptions and the coma thermal emission features of active comets is very complex. For these reasons, they have been excluded from the analysis. The all-sky map in Fig. 6 shows the increment in antenna temperature in *Planck*'s 30-GHz channel due to the thermal emission of all planets and asteroids considered.

4.7 Future work concerning *Planck*'s foregrounds

Foreground components not considered so far include microwave point sources, such as infrared galaxies and microwave emitting active galactic nuclei (AGNs). The emission of infrared galaxies is associated with absorption of starlight by dust and re-emission at longer wavelengths. Galaxies with ongoing star formation can have large fractions (∼90 per cent) of their total emission at infrared wavelengths, compared to about one-third in the case of local galaxies. The integrated emission from unresolved infrared galaxies accounts for the cosmic infrared background (Puget et al. 1996; Lagache & Puget 2000), the fluctuations of which are impeding SZ observations at frequencies above $\nu \simeq 100$ GHz (Aghanim, Hansen & Lagache 2005).

Lagache (2003) and White & Majumdar (2004) have estimated the number counts of unresolved infrared galaxies at *Planck* frequencies, which was used by Aghanim et al. (2005) in order to estimate the level of fluctuation in the *Planck* beam. In the easiest case, the sources are uncorrelated and the fluctuations obey Poissonian statistics, but the inclusion of correlations is expected to boost the fluctuations by a factor of ∼1.7 (Song et al. 2003). According to Aghanim et al. (2005), the resulting fluctuations vary between a few 10^2 and 10^5 Jy sr^{-1}, depending on observing channel.

---

[3] http://cfa-www.harvard.edu/cfa/ps/mpc.html

A proper modelling would involve a biasing scheme for populating haloes, the knowledge of the star formation history and template spectra in order to determine the *K*-corrections.

AGNs are another extragalactic source of submillimetric emission. Here, synchrotron emission is the radiation generating mechanism. The spectra show a variety of functional behaviours, with spectral indices α generally ranging from -1 to -0.5, but sources with inverted spectra $\alpha > 0$ are commonplace. This variety makes it difficult to extrapolate fluxes to observing frequencies of CMB experiments. Two studies (Toffolatti et al. 1998; Sokasian, Gawiser & Smoot 2001) have estimated the fluctuations generated by radio emitting AGNs at SZ frequencies and found them to amount to 10^3–10^4 Jy sr^{-1}. However, AGNs are known to reside in high-density environments and the proper modelling would involve a (poorly known) biasing scheme in order to assign AGN to the dark matter haloes. Apart from that, one would have to assume spectral properties from a wide range of spectral indices and AGN activity duty cycles. Therefore, the study of extragalactic sources has been omitted from this analysis.

Yet another source of microwave emission in the Solar system is the zodiacal light (Leinert et al. 2002; Reach et al. 2003; Maris, Burigana & Fogliani 2006). Modelling of this emission component is very difficult due to the Lissajous orbit of *Planck* around the Lagrangian point L_2. The disc of interplanetary dust is viewed under varying angles depending on the orbital period and the integration over the spatially non-uniform emission features is very complicated. Reach et al. (2003) have investigated the thermal emission by interplanetary dust from measurements by *ISO* and have found dust temperatures of $T_{zodiacal} = 250$–300 K and fluxes on the level of $\simeq 10^3$ Jy sr^{-1}, i.e. the equilibrium temperature is separated by two orders of magnitude from the CMB temperature, which means that the intensities are suppressed by a factor of $\sim 10^4$ due to the Rayleigh–Jeans regime of the zodiacal emission in which *Planck* is observing and by a factor of 10^5 due to *Planck*'s narrow beams. From this it is concluded that the emission from zodiacal light is unlikely to exceed values of a few μJy in observations by *Planck* which compares to the fluxes generated by faint asteroids. Thus, the zodiacal light constitutes only a weak foreground emission component at submillimetric wavelengths and can safely be neglected.

There are claims of yet another Galactic emission component: the emission of spinning dust as discussed in Draine & Lazarian (1998). Spinning dust should be most important at low frequencies, but extragalactic observations of a number of galaxies yielded no evidence so far (Bennett et al. 2003b).

5 SIMULATING SZ OBSERVATIONS BY *PLANCK*

The simulation for assessing *Planck*'s SZ capabilities proceeds in four steps. First, all-sky maps of the thermal and kinetic SZ effects are prepared, the details of map construction are given in Section 5.1. Secondly, a realization of the CMB was prepared for the assumed cosmological model (Section 5.2). The amplitudes were co-added with the Galactic and ecliptic foregrounds introduced in the previous section, subsequently degraded in resolution with *Planck*'s beams (Section 5.3). Finally, uncorrelated pixel noise as well as the emission maps comprising planets and asteroids were added. In the last section, cross-correlation properties of the various astrophysical and instrumental noise components are discussed (Section 5.4).

At this stage it should be emphasized that we work exclusively with spherical harmonics expansion coefficients $a_{\ell m}$ of the flux maps. The expansion of a function $a(\theta)$ into spherical harmonics

$Y_\ell^m(\theta)$ and the corresponding inversion is given by

$$a_{\ell m} = \int d\Omega \, a(\theta) \, Y_\ell^m(\theta)^* \quad \text{and} \quad a(\theta) = \sum_{\ell=0}^{\infty} \sum_{m=-\ell}^{+\ell} a_{\ell m} Y_\ell^m(\theta). \tag{26}$$

Here, $d\Omega$ denotes the differential solid angle element. For reasons of computational feasibility, we assume isotropic spectral properties of each emission component, i.e. the template map is only providing the amplitude of the respective emission component, but the spectral dependences are assumed to remain the same throughout the sky. While this is an excellent approximation for the CMB and the SZ effects (in the non-relativistic limit), this assumption is seriously challenged in the case of Galactic foregrounds, where the spectral laws show significant spatial variations. The synchrotron spectral index assumes values in the interval $\gamma = -0.5$ to -1.2 as derived by Giardino et al. (2002) from measurements at $\nu = 408$ MHz and $\nu = 2.326$ GHz. This would result in differences amounting to about an order of magnitude when extrapolating to the lowest *Planck* frequencies, but the result from Giardino et al. (2002) is in contradiction to the recent *WMAP* foreground studies (Bennett et al. 2003b). Similarly, the plasma temperature T_p which is the parameter determining the free–free emission strength, varies between 4×10^3 and 15×10^3 K which changes the conversion from Hα intensity to fluxes by a factor of slightly above 2. It should be emphasized, however, that the filter schemes discussed in Section 6 do work irrespective of this assumption.

Adopting this approximation, the steps in constructing spherical harmonics expansion coefficients $\langle S_{\ell m} \rangle_{\nu_0}$ of the flux maps $S(\theta, \nu)$ for all *Planck* channels consist of deriving the expansion coefficients of the template, converting the template amplitudes to flux units, extrapolate the fluxes with a known or assumed spectral emission law to *Planck*'s observing frequencies, to finally convolve the emission law with *Planck*'s frequency response window for computing the spherical harmonics expansion coefficients of the average measured flux $\langle S_{\ell m} \rangle_{\nu_0}$ at nominal frequency ν_0 by using equation (27).

$$\langle S_{\ell m} \rangle_{\nu_0} = \frac{\int d\nu \, S_{\ell m}(\nu) R_{\nu_0}(\nu)}{\int d\nu \, R_{\nu_0}(\nu)} = 2 \frac{\nu_0^2}{c^2} k_B T_{\ell m}. \tag{27}$$

Here, $S_{\ell m}(\nu)$ describes the spectral dependence of the emission component considered, and $R_{\nu_0}(\nu)$ the frequency response of *Planck*'s receivers centred on the fiducial frequency ν_0. Assuming spatial homogeneity of the spectral behaviour of each emission component it is possible to decompose $S_{\ell m}(\nu)$ into $S_{\ell m}(\nu) = q(\nu) \, a_{\ell m}$, i.e. a frequency dependent function $q(\nu)$ and the spherical harmonics expansion coefficients $a_{\ell m}$ of the template describing the morphology. This is possible due to the fact that the decomposition equation (26) is linear. Additionally, equation (27) gives the conversion from the averaged flux $\langle S_{\ell m} \rangle_\nu$ in a *Planck* channel to antenna temperature $T_{\ell m}$.

Planck's frequency response function $R_{\nu_0}(\nu)$ is well approximated by a top-hat function:

$$R_{\nu_0}(\nu) = \begin{cases} 1, & \nu \in [\nu_0 - \Delta\nu, \nu_0 + \Delta\nu] \\ 0, & \nu \notin [\nu_0 - \Delta\nu, \nu_0 + \Delta\nu] \end{cases} . \tag{28}$$

The centre frequencies ν_0 and frequency windows $\Delta\nu$ for *Planck*'s receivers are summarized in Table 1. In this way it is possible to derive a channel-dependent prefactor relating the flux expansion coefficients $\langle S_{\ell m} \rangle_{\nu_0}$ to the template expansion coefficients $A_{\ell m}$. The superposition of the various emission components in spherical harmonics and the determination of response-folded fluxes is most

conveniently done using the almmixer utility of *Planck*'s simulation package. The wide frequency windows do not significantly complicate the SZ measurements due to the slow variation of the SZ effect with frequency. Consequently, the window-convolved SZ fluxes differ by a few per cent from the unconvolved SZ spectrum, as discussed previously by Church, Knox & White (2003).

5.1 SZ map preparation

For constructing an all-sky SZ map, a hybrid approach has been pursued. Due to the SZ clusters being detectable out to very large redshifts, due to their clustering properties on very large angular scales, and due to the requirement of reducing cosmic variance when simulating all-sky observations as will be performed by *Planck*, there is the need for very large simulation boxes, encompassing redshifts of $z \simeq 1$ which corresponds to comoving scales exceeding $2\,\mathrm{Gpc}$. Unfortunately, a simulation incorporating dark matter and gas dynamics that covers cosmological scales of that size down to cluster scales and possibly resolving cluster substructure is beyond computational feasibility. For that reason, two simulations have been combined: the Hubble-volume simulation (Colberg et al. 2000; Jenkins et al. 2001), and a smaller-scale simulation including (adiabatic) gas physics by White, Hernquist & Springel (2002) performed with GADGET (Springel, Yoshida & White 2001; Springel & Hernquist 2002).

All-sky maps of the SZ sky were constructed by using the light-cone output of the Hubble-volume simulation as a cluster catalogue and template clusters from the small-scale gas-dynamical simulation. In this way, the sky maps contain all clusters above $5 \times 10^{13}\,\mathrm{M_\odot}\,h^{-1}$ out to redshift $z = 1.48$. The analysis undertaken by Bartelmann (2001) gives expected mass and redshift ranges for detectable thermal SZ clusters, which are covered completely by the all-sky SZ map presented here. The maps show the correct two-point halo correlation function, incorporate the evolution of the mass function and the correct distribution of angular sizes.

Furthermore, they exhibit cluster substructure and deviations from the ideal cluster scaling relations induced by the departure from spherical symmetry. The velocities used for computing the kinetic SZ effect correspond to the ambient density field. The map construction process and the properties of the resulting map are in detail described in Schäfer et al. (2004). Visual impressions of the SZ maps are given by Figs 7 and 8.

The fluxes generated by the thermal SZ effect $S_{\mathcal{Y}}(x)$ and of the kinetic SZ effect $S_{\mathcal{W}}(x)$ are given by equations (29) and (30), respectively. The dimensionless frequency is defined as $x = h\nu/(k_\mathrm{B} T_\mathrm{CMB})$ and the flux density of the CMB is given by $S_0 = (k_\mathrm{b} T_\mathrm{CMB})^3 \pi^3/c^2/h^2/5400 = 22.9\,\mathrm{Jy\,arcmin}^{-2}$.

$$S_{\mathcal{Y}}(x) = S_0\,\mathcal{Y}\,\frac{x^4\,\exp(x)}{[\exp(x)-1]^2}\left[x\,\frac{\exp(x)+1}{\exp(x)-1} - 4\right]. \tag{29}$$

$$S_{\mathcal{W}}(x) = S_0\,\mathcal{W}\,\frac{x^4\,\exp(x)}{[\exp(x)-1]^2}. \tag{30}$$

Table 1 summarizes the fluxes $S_{\mathcal{Y}}$ and $S_{\mathcal{W}}$ and the corresponding changes in antenna temperature $T_{\mathcal{Y}}$ and $T_{\mathcal{W}}$ for the respective Comptonization of $\mathcal{Y} = \mathcal{W} = 1\,\mathrm{arcmin}^2$ for all *Planck* channels.

Fig. 9 shows how the frequency dependence of the SZ signal is altered by *Planck*'s relatively broad frequency response functions. The relative deviations of curves in which the frequency window has been taken into account to the unaltered curve amounts to 5–15 per cent, depending on observation frequency.
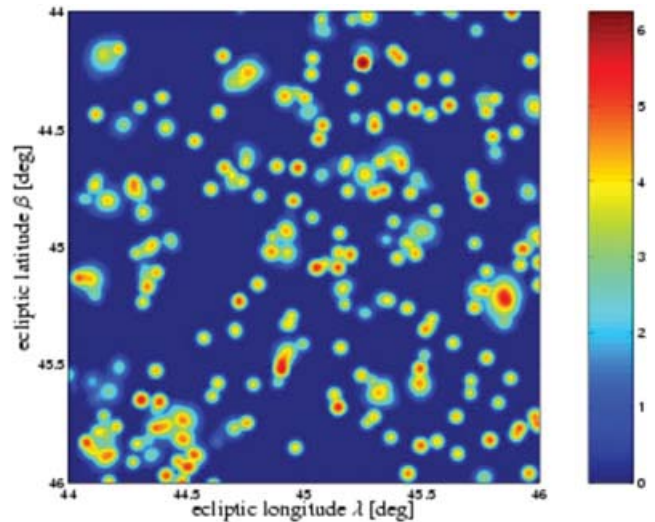

Figure 7. Detail of the thermal Comptonization map: a 2×2-deg^2 wide cut-out centred on the ecliptic coordinates $(\lambda, \beta) = (45°, 45°)$ is shown. The smoothing imposed was a Gaussian kernel with $\Delta\theta = 2.0$ arcmin (FWHM). The shading indicates the value of the thermal Comptonization y, which is proportional to arsinh $(10^6 y)$. This map resulted from a projection on a Cartesian grid with mesh size ~14 arcsec, i.e. no HEALPix pixelization can be seen.

5.2 CMB map generation

The angular power spectrum C_ℓ is computed for a flat ΛCDM cosmology using the CMBFAST code by Seljak & Zaldarriaga (1996). In addition to the cosmological parameters being already given in Section 1, we use adiabatic initial conditions, set the CMB monopole to $T_\mathrm{CMB} = 2.725$ K (Mather et al. 1999) and the primordial He mass fraction to $X_\mathrm{He} = 0.24$. The reionization optical depth τ was set to $\tau = 0.17$ and the reionization redshift was taken to be $z_\mathrm{reion} = 20$ (Bennett et al. 2003a). The angular power spectrum of the CMB is normalized to *COBE* data. With the spectrum of C_ℓ coefficients, a set of $a_{\ell m}$ coefficients was synthesized by using the SYNALM code
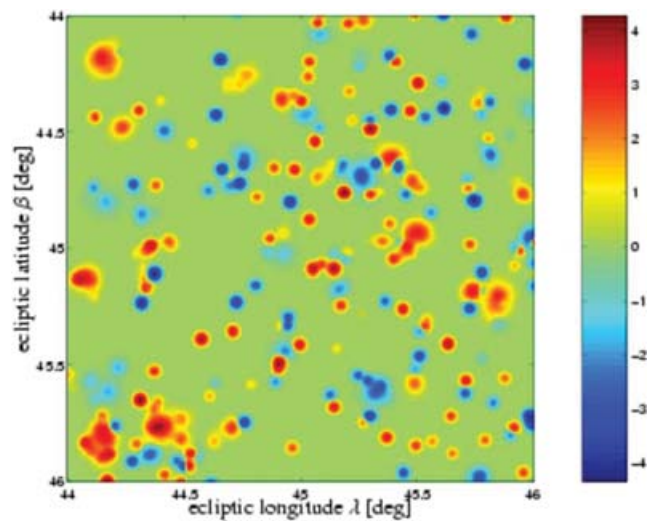
Figure 8. Detail of the kinetic Comptonization map: a 2×2-deg^2 wide cut-out centred on the same position as Fig. 7, i.e. at the ecliptic coordinates $(\lambda, \beta) = (45°, 45°)$ is shown. The smoothing imposed was a Gaussian kernel with $\Delta\theta = 2.0$ arcmin (FWHM). The kinetic Comptonization w is indicated by the shading, being proportional to arsinh $(10^6 w)$.
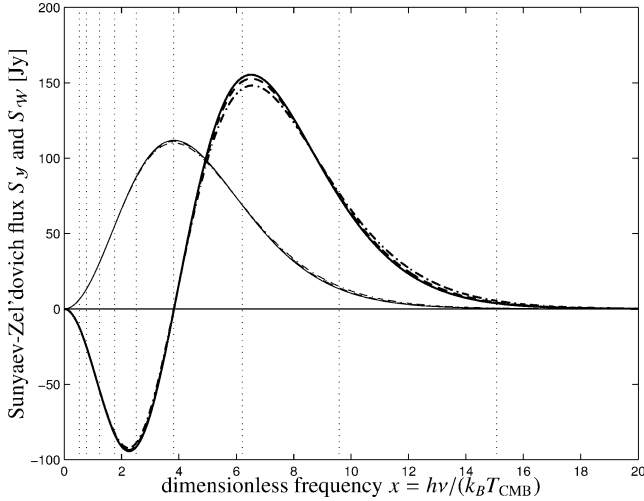
Figure 9. Frequency dependence of the thermal (thick lines) and of the kinetic SZ flux (thin lines), for ideal δ-like frequency responses (solid lines), for a top-hat window function with a relative width of 10 per cent corresponding to *Planck*'s LFI instrument and for a top-hat window function with a relative width of 16.7 per cent, as planned for *Planck*'s HFI instrument. The fluxes stated correspond to the integrated Comptonization of $\mathcal{Y} = \mathcal{W} = 1$ arcmin^2. The vertical lines indicate the centre frequencies of *Planck*'s receivers.

based on SYNFAST by Hivon, Wandelt & Gorski (1998). The factors for converting the $a_{\ell m}$ coefficients of the CMB map showing the thermodynamic temperature and to the corresponding fluxes for each channel were then derived by convolution of the Planckian emission law equation (31),

$$S_{\text{CMB}}(\nu) = S_0 \frac{x^3}{\exp(x) - 1}, \tag{31}$$

with *Planck*'s frequency response function equations (27) and (28). Again, $S_0 = 22.9$ Jy arcmin^{-2} is the energy flux density of the CMB.

5.3 Preparation of simulation data sets

The expansion coefficients of the flux maps are multiplied with the respective beam's $b_{\ell 0}$ coefficients in order to describe the finite angular resolution. After that, expansion coefficients of the pixel noise maps and those of the planetary maps have been added. In total, three atlases consisting of nine flux $\langle S_{\ell m} \rangle_{\nu_0}$ sets belonging to each of *Planck*'s channels with fiducial frequency ν_0 have been compiled.

(i) The reference data set is a combination of the CMB, the SZ maps and the instrumental noise maps. They should provide the cleanest detection of clusters and the measurement of their properties. Apart from the inevitable instrumental noise, this data set only contains cosmological components. In the remainder of the paper, this data set will be referred to as COS.

(ii) The second data set adds Galactic foregrounds to the CMB, the SZ maps and the instrumental noise map. Here, we try to assess the extend to which Galactic foregrounds impede the SZ observations. Thus, this data set will be denoted GAL.

(iii) In the third data set the emission from bodies inside the Solar system was included to the CMB, the SZ maps, the Galactic foregrounds and the instrumental noise. Because of the planets and asteroids being loosely constrained to the ecliptic plane, this data set will be called ECL.
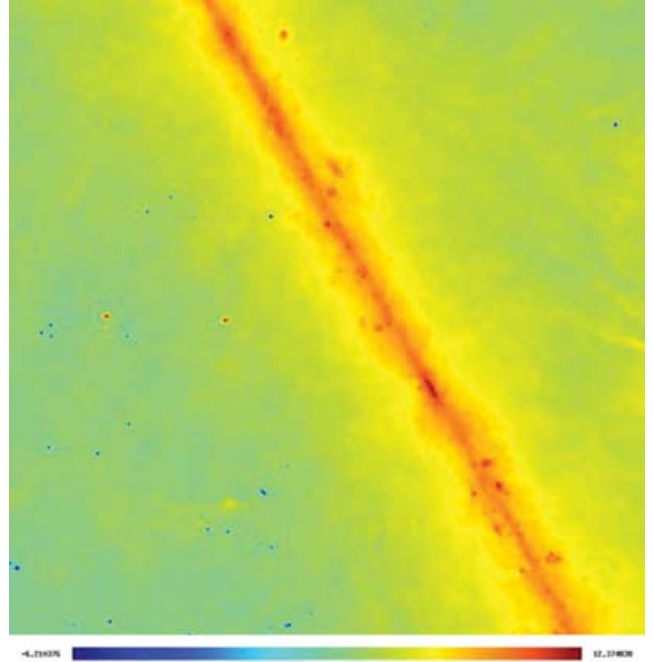
Figure 10. A 50×50-deg^2 wide composite centred on the ecliptic coordinates $(\lambda, \beta) = (-85°, 0°)$, i.e. close to the Galactic centre for *Planck*'s $\nu = 143$ GHz channel. The shading is proportional to arsinh $(T_A(\nu = 143 \text{ GHz}) \mu\text{K}^{-1})$. The map is smoothed with the corresponding beam of diameter $\Delta\theta = 7.1$ arcmin (FWHM). SZ clusters are observed in absorption in this channel and are discernible by eye even at close proximity $(b \lesssim 20°)$ to the Galactic plane. For clarity, the CMB fluctuations as well as the instrumental noise have been excluded. The two point sources on the ecliptic equator are twin detections of Jupiter.

An example of a synthesized map showing the combined emission of the SZ clusters and all Galactic and ecliptic components including neither CMB fluctuations nor instrumental noise at a location close to the Galactic plane is given by Fig. 10. The observing frequency has been chosen to be $\nu = 143$ GHz, correspondingly, the map has been smoothed with a (Gaussian) beam of $\Delta\theta = 7.1$ arcmin (FWHM).

5.4 *Planck* channel correlation properties

In this section the autocorrelation as well as the cross-correlation properties of the various foregrounds in different *Planck* channels are studied. The cross-power spectra, defined formally by equation (37) are determined by using

$$C_{\ell,\nu_1\nu_2} = \frac{1}{2\ell + 1} \sum_{m=-\ell}^{+\ell} \langle S_{\ell m} \rangle_{\nu_1} \langle S_{\ell m} \rangle_{\nu_2}^*. \tag{32}$$

From this definition, the autocorrelation spectra are obtained by setting $\nu_1 = \nu_2$, i.e. $C_{\ell,\nu} = C_{\ell,\nu\nu}$. The band-pass-averaged fluxes $\langle S_{\ell m} \rangle_\nu$ are defined in equation (27). In Fig. 11, the power spectra are shown for the $\nu = 30, 143, 353$ and 847 channels. The spectra have been derived including various Galactic and ecliptic noise components in order to study their relative influences. For visualization purposes, the spectra are smoothed with a moving average filter with a filter window comprising 11 bins.
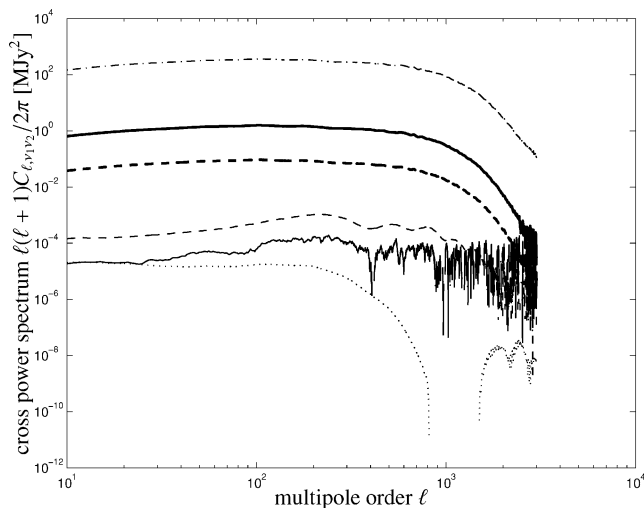
Distinct acoustic peaks of the CMB are clearly visible in the clean COS data sets, but are overwhelmed by the Galactic noise components. At small scales, i.e. high multipole order ℓ, differences between the GAL and ECL data sets become apparent, the
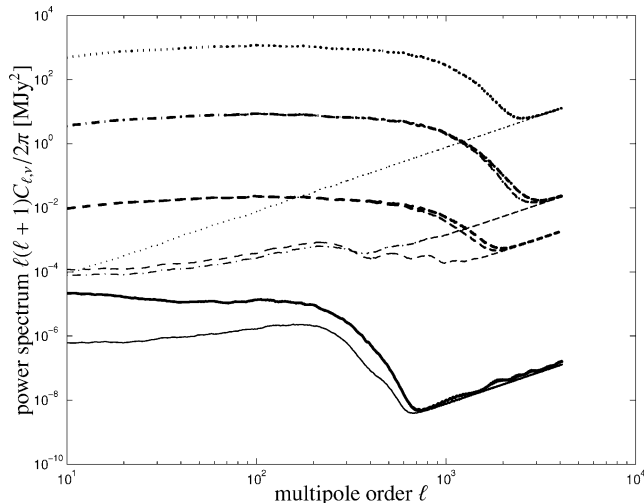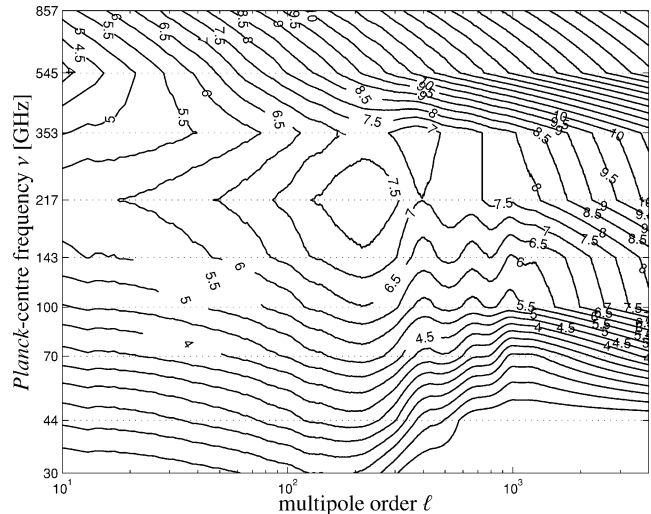
Figure 11. Power spectra in various *Planck* channels: $\nu = 30\,\mathrm{GHz}$ (solid), $\nu = 143\,\mathrm{GHz}$ (dashed), $\nu = 353\,\mathrm{GHz}$ (dash–dotted) and $\nu = 857\,\mathrm{GHz}$ (dotted) for COS data set (thin line), the GAL data set (medium line) and the ECL data set (thick line).

Figure 13. Autocorrelations: the power spectral $C_{\ell,\nu}$ coefficients are shown as a function of observing frequency ν and multipole order ℓ in the usual representation $\ell(\ell+1)C_{\ell,\nu}/2\pi$. The amplitudes are given in $\mu\mathrm{K}^2$ and the contours are linearly spaced. Note the logarithmic scaling of the frequency axis. In the data set displayed, the CMB, both SZ effects and instrumental noise are included. The first three acoustic oscillation peaks are clearly visible.

latter showing a higher amplitude. The (single) acoustic peak measurable in the $\nu = 33\,\mathrm{GHz}$ channel is shifted to larger angular scales due to the coarse angular resolution of that particular channel. The $\nu = 857\,\mathrm{GHz}$ curve of the COS data set behaves like a power law due to the fact that the CMB is observed in the Wien regime and is consequently strongly suppressed, such that the angular power spectrum is dominated by uncorrelated pixel noise.

Fig. 12 shows exemplarily a couple of cross-power spectra. The cross-correlation spectra derived for the COS data set nicely shows the CMB power spectrum if two neighbouring channels close to the CMB maximum are chosen, but the correlation is lost in two widely separated channels. This is especially the case if one considers the two lowest LFI channels at angular scales which the receivers are
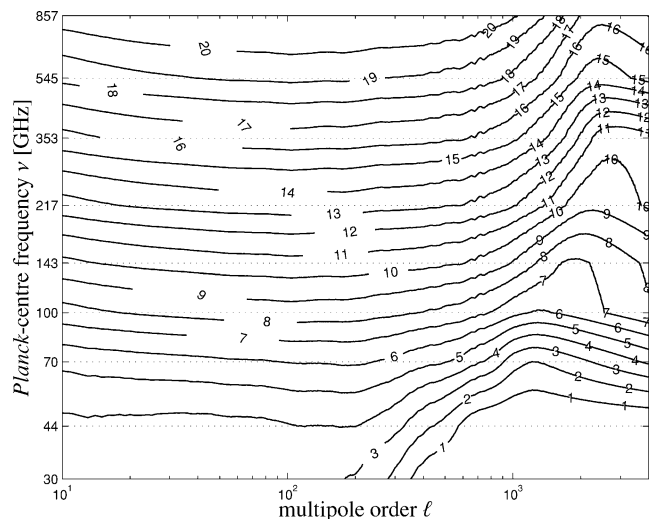
not able to resolve. In this regime the pixel noise is still very small and the cross-correlation spectrum drops to very small values.

In order to illustrate the complexity of spectral and morphological behaviour of the power spectra, they are given as contour plots depending on both the observing frequency ν and the multipole order ℓ. Figs 13 and 14 contrast the autocorrelation properties of the different data sets. The COS data set, shown in Fig. 13, containing nothing but the CMB and instrumental noise apart from the SZ contribution, shows clearly the acoustic oscillations with the first peak at $\ell \simeq 200$ and the consecutive higher harmonics. They are most pronounced in the $\nu = 100$ and $143\,\mathrm{GHz}$ channels. At higher

Figure 12. Cross-correlations: the spectra $C_{\ell,\nu_1=143\mathrm{GHz},\nu_2=545\mathrm{GHz}}$ (solid line) and $C_{\ell,\nu_1=143\mathrm{GHz},\nu_2=217\mathrm{GHz}}$ (dashed line) are contrasted for the COS data set (thin lines) versus the GAL data set (thick line). Furthermore, the spectrum $C_{\ell,\nu_1=545\mathrm{GHz},\nu_2=857\mathrm{GHz}}$ (dash- -dotted line) as well as $C_{\ell,\nu_1=30\mathrm{GHz},\nu_2=44\mathrm{GHz}}$ (dotted line) is shown as derived from the ECL data set.

Figure 14. Autocorrelations: the power spectral $C_{\ell,\nu}$ coefficients are shown as a function of observing frequency ν and multipole order ℓ in the usual representation $\ell(\ell+1)C_{\ell,\nu}/2\pi$. The amplitudes are given in $\log(\mu\mathrm{K}^2)$ with logarithmically equidistant contours. In the data set displayed, the CMB, both SZ effects, all Galactic foregrounds and instrumental noise are included.

multipole moments, the power spectra are dominated by instrumental noise which leads to a rapid (power-law) incline.

Adding Galactic foregrounds yields the spectra depicted in Fig. 14. Inclusion of Galactic foregrounds significantly complicates the picture and masks off the primary anisotropies. The spectra are dominated by large-scale emission structures of the Milky Way, most notably the emission from thermal dust that causes the spectra to increase with increasing frequency ν.

6 CLUSTER DETECTION BY USING MULTIFREQUENCY OPTIMIZED FILTERING

One challenge in the analysis of two-dimensional all-sky surveys is the extraction of sources of interest which are superposed on a background of noise of varying morphology and spectral behaviour. In the presence of small-scale noise the conventional method to extract sources is low-pass filtering (e.g. with a Gaussian kernel) while wavelet analysis is most suitably applied if large-scale noise fluctuations dominate. These methods, however, fail if the characteristic scale of the background fluctuations is comparable with the scale of the signal structures. Other methods have been proposed in order to separate different components in multifrequency CMB observations: they include Wiener filtering (Tegmark & Efstathiou 1996; Bouchet & Gispert 1999; Bouchet, Prunet & Sethi 1999), maximum-entropy methods (Hobson et al. 1998, 1999), Mexican-hat wavelet analysis (Cayón et al. 2000; Vielva et al. 2001a), fast independent component analysis (Maino et al. 2002), matched filter analysis (Tegmark & de Oliveira-Costa 1998), adaptive filtering techniques (Sanz et al. 2001; Herranz et al. 2002a,b) and non-parametric Bayesian approaches (Diego et al. 2002).

However, a comparison between these methods is difficult because they all assume different priors about the spatial properties and frequency dependence. Using prior knowledge about the frequency dependence and statistical properties of several images at different channels, the maximum-entropy method and Wiener filtering are able to separate the components of interest. Contrarily, wavelet analysis is well suited in order to detect compact sources. A combination of these different techniques improves the quality of component separation (Vielva et al. 2001b). Although component separation methods which assume a prior knowledge about the data are quite powerful, they yield biased or even wrong results in the case of incorrect or idealized assumptions about the data. Any error in the separation of one component propagates to the separation of the other components owing to normalization constraints. In particular, this is the case in non-centrally symmetric source profiles, oversimplified spectral extrapolations of Galactic emission surveys into other wavebands, variations of the assumed frequency dependence, or non-Gaussian noise properties the statistics of which can not fully be characterized by power spectra. Thus, the application of a specific component separation method is a trade-off between robustness and effectiveness with regard to the particular problem.

Filtering techniques relying on Mexican-hat wavelets and on matched and scale-adaptive filters are single component separation methods. They all project either spatial structure or frequency properties (within a given functional family) of the component of interest in the presence of other components acting as background in this context. While Mexican-hat wavelet analysis assumes Gaussian profiles superimposed on large-scale variations of the background noise, the matched and scale-adaptive filter generalizes to arbitrary source profiles and noise properties which are assumed to be locally homogeneous and isotropic (Sanz et al. 2001; Herranz et al. 2002a,b).

This section generalizes the matched and scale-adaptive filter techniques to global spherical topologies which find application in all-sky surveys such as the case of *Planck*'s microwave/submillimetric survey. In addition, optimized filters for the detection of compact sources in single frequency all-sky observations are derived in Appendix A in a more detailed fashion. The proposed method aims at simultaneously localizing SZ clusters and measuring both their amplitudes and angular extent. It can also be applied for localizing microwave point sources and estimating their spectral properties.

We choose the spherical filtering approach rather than tiling the sky with a set of two-dimensional flat maps for the following reasons. On the sphere, we do not have to worry about double detections due to overlaps in the tesselation. Secondly, our approach provides a physical interpretation of our filter shapes in harmonic space even for the smallest multipole moments in contrast to the case of a flat map where the smallest wavenumbers are determined by the map size. Finally, our approach circumvents projection failures of the noise properties such as stretching effects in the case of conformal mapping which would introduce artificial non-Gaussianity in our maps and distort profile shapes close to the map boundaries.

We pursue the concept of the *multifrequency approach* rather than the *combination method* (cf. Herranz et al. 2002a). In other words, we filter each channel separately while taking into account the different cross-correlations between the different channels and the frequency dependence of the signal when constructing the optimized filters. This method seems to be superior to the *combination method* which tries to find an optimized combination of the different channels with regard to the signal-to-noise ratio of the sources and successively applies filters to the combined map.

The concept is introduced and central definitions are laid down in Section 6.1. The concept of constructing filter kernels is outlined in Section 6.2. Subsequently, the matched and scale-adaptive filters are derived for expansions of spherical data sets into spherical harmonics in Sections 6.3 and 6.4. Then, the numbers of merit are defined in Section 6.5. Caveats in the numerical derivation are listed in Section 6.6. A discussion of filter kernel shapes in Section 6.7 for actual simulation data. The application of the filter kernels to our simulated sky maps and the extraction of the SZ cluster signal is described in Section 6.8.

6.1 Assumptions and definitions

When constructing the particular filters, we assume centrally symmetric profiles of the sources to be detected. This approximation is justified for most of the clusters of *Planck*'s sample whose angular extent will be comparable in size to *Planck*'s beams, i.e. the instrumental beam renders them azimuthally symmetric irrespective of their intrinsic shape. Azimuthal symmetry is no general requirement for the filters which can be generalized to detect, for example, elliptic clusters using expansions into vector rather than scalar spherical harmonics.

We furthermore assume the background to be statistically homogeneous and isotropic, i.e. a complete characterization can be given in terms of the power spectrum. This assumption obviously fails for non-Gaussian emission features of the Galaxy or of the exposure-weighted instrumental noise on large angular scales. However, the spherical harmonics expansion of any expected compact source profile, which we aim to separate, peaks at high values of the multipole moment due to the smallness of the clusters where the non-Gaussian influence is negligible. Thus, we only have to require homogeneity and isotropy of the background on small scales.

In order to construct our filters, we consider a set of all-sky maps of the detected scalar field $s_\nu(\theta)$ for the different frequency channels

$$s_\nu(\theta) = f_\nu y_\nu(|\theta - \theta_0|) + n_\nu(\theta), \quad \nu = 1, \ldots, N, \tag{33}$$

where $\theta = (\vartheta, \varphi)$ denotes a two-dimensional vector on the sphere, θ_0 is the source location, and N is the number of frequencies (respectively, the number of maps). The first term on the right-hand side represents the amplitude of the signal caused by the thermal and kinetic SZ effect, $y(|\theta - \theta_0|)$ and $w(|\theta - \theta_0|)$, respectively, while the second term corresponds to the generalized noise which is composed of CMB radiation, all Galactic and ecliptic emission components, and additional instrumental noise. The frequency dependence of the SZ effect is described by f_ν in terms of average flux

$$f_\nu \equiv \langle S_\mathcal{Y} \rangle_\nu \quad \text{and} \quad f_\nu \equiv \langle S_\mathcal{W} \rangle_\nu, \tag{34}$$

where $\langle S \rangle_\nu$ denotes the flux weighted by the frequency response at the fiducial frequency ν (cf. equation 27) and $S_\mathcal{Y}$ and $S_\mathcal{W}$ denote the SZ fluxes given by equations (29) and (30).

We expect a multitude of clusters to be present in our all-sky maps. In order to sketch the construction of the optimized filter, we assume an individual cluster situated at the North pole ($\theta_0 = \mathbf{0}$) with a characteristic angular SZ signal $y_\nu(\theta = |\theta|) = A\tau_\nu(\theta)$, where we separate the true amplitude A and the spatial profile normalized to unity, $\tau_\nu(\theta)$. The underlying cluster profile $p(\theta)$ is assumed to follow a generalized King profile with an exponent λ which is a parameter in our analysis. At each observation frequency this profile is convolved with the (Gaussian) beam of the respective *Planck* channel (cf. Section 3.1) yielding

$$\tau_\nu(\theta) = \int d\Omega' \, p(\theta') b_\nu(|\theta - \theta'|) = \sum_{\ell=0}^{\infty} \tau_{\ell 0, \nu} Y_\ell^0(\cos\theta), \tag{35}$$

$$p(\theta) = \left[1 + \left(\frac{\theta}{\theta_c}\right)^2\right]^{-\lambda} \quad \text{and} \quad \tau_{\ell 0, \nu} = \sqrt{\frac{4\pi}{2\ell + 1}} b_{\ell 0, \nu} p_{\ell 0}. \tag{36}$$

For the second step in equation (36) we used the convolution theorem on the sphere to be derived in Appendix A. The background $n_\nu(\theta)$ is assumed to be a compensated homogeneous and isotropic random field with a cross-power spectrum $C_{\ell, \nu_1 \nu_2}$ defined by

$$\left\langle n_{\ell m, \nu_1} n^*_{\ell' m', \nu_2} \right\rangle = C_{\ell, \nu_1 \nu_2} \delta_{\ell\ell'} \delta_{mm'}, \quad \text{where} \quad \langle n_\nu(\theta) \rangle = 0, \tag{37}$$

$n_{\ell m, \nu}$ denotes the spherical harmonics expansion coefficient of $n_\nu(\theta)$, $\delta_{\ell\ell'}$ denotes the Kronecker symbol and $\langle \cdot \rangle$ corresponds to an ensemble average. Assuming ergodicity of the field under consideration allows taking spatial averages over sufficiently large areas $\Omega = \mathcal{O}(4\pi)$ instead of performing the ensemble average.

The construction of the filter kernel for the optimized detection of a generalized King profile $p(\theta)$ with the parameters θ_c and λ is motivated by a simple analytic formula that is known to be a fair description of a cluster's thermal SZ profile. One can expect that asymmetric clusters will yield a smaller amplitude in the filtered map than a spherically symmetric system with the same integrated Comptonization. In the interesting case of clusters with pronounced substructure or bimodal morphology it is obvious that these peaks merge when convolved with kernels optimized for finding extended systems (i.e. large θ_c and small λ).

6.2 Concepts in filter construction

The idea of an optimized matched filter for multifrequency observations was recently proposed by Herranz et al. (2002a) for the case of a

flat geometry. For each observing frequency, we aim at constructing a centrally symmetric optimized filter function $\psi_\nu(\theta)$ operating on a sphere. Its functional behaviour induces a family of filters $\psi_\nu(\theta, R_\nu)$ which differ only by a scaling parameter R_ν. For a particular choice of this parameter, we define the filtered field $u_\nu(R_\nu, \beta)$ to be the convolution of the filter function with the observed all-sky map at frequency ν,

$$u_\nu(R_\nu, \beta) = \int d\Omega \, s_\nu(\theta) \, \psi_\nu(|\theta - \beta|, R_\nu) \tag{38}$$

$$= \sum_{\ell=0}^{\infty} \sum_{m=-\ell}^{+\ell} u_{\ell m, \nu} Y_\ell^m(\beta) \quad \text{with} \tag{39}$$

$$u_{\ell m, \nu} = \sqrt{\frac{4\pi}{2\ell + 1}} s_{\ell m, \nu} \, \psi_{\ell 0, \nu}(R_\nu). \tag{40}$$

For the second step, the convolution theorem to be derived in Appendix A was used. The combined filtered field is defined by

$$u(R_1, \ldots, R_N; \beta) = \sum_\nu u_\nu(R_\nu, \beta). \tag{41}$$

Taking into account the vanishing expectation value of the noise $\langle n_\nu(\theta) \rangle = 0$, the expectation value of the filtered field at the North pole $\beta = \mathbf{0}$ is given by

$$\langle u_\nu(R_\nu, \mathbf{0}) \rangle = A f_\nu \sum_{\ell=0}^{\infty} \tau_{\ell 0, \nu} \, \psi_{\ell 0, \nu}(R_\nu). \tag{42}$$

The assumption that the cross-power spectrum of the signal is negligible compared to the noise power spectrum is justified because the thermal and kinetic amplitudes are small compared to unity, $A_{y,w} \ll 1$. Thus, the variance of the combined filtered field (41) is determined by

$$\sigma_u^2(R_1, \ldots, R_N) = \left\langle [u(R_1, \ldots, R_N; \beta) - \langle u(R_1, \ldots, R_N; \beta) \rangle]^2 \right\rangle$$

$$= \sum_{\nu_1, \nu_2} \sum_{\ell=0}^{\infty} C_{\ell, \nu_1 \nu_2} \psi_{\ell 0, \nu_1}(R_{\nu_1}) \psi_{\ell 0, \nu_2}(R_{\nu_2}). \tag{43}$$

The optimized filter functions $\psi_\nu(\theta)$ are chosen to detect the clusters at the North pole of the sphere (to which they have been translated). They are described by a singly peaked profile which is characterized by the scale $R_\nu^{(0)}$ as given by equation (35). While the optimized *matched filter* is defined to obey the first two of the following conditions, the optimized *scale-adaptive filter* is required to obey all three conditions.

(i) The combined filtered field $u(R_1^{(0)}, \ldots, R_N^{(0)}; \mathbf{0})$ is an unbiased estimator of the source amplitude A, i.e. $\langle u(R_1^{(0)}, \ldots, R_N^{(0)}; \mathbf{0}) \rangle = A$.

(ii) The variance of $u(R_1, \ldots, R_N; \beta)$ has a minimum at the scales $R_1^{(0)}, \ldots, R_N^{(0)}$ ensuring that the combined filtered field is an efficient estimator.

(iii) The expectation value of the filtered field at the source position has an extremum with respect to the scale $R_\nu^{(0)}$, implying

$$\frac{\partial}{\partial R_\nu^{(0)}} \langle u_\nu(R_\nu, \mathbf{0}) \rangle = 0. \tag{44}$$

6.3 Matched filter

For convenience, we introduce the column vectors $\boldsymbol{\psi}_\ell \equiv [\psi_{\ell 0, \nu}]$, $\mathbf{F}_\ell \equiv [f_\nu \tau_{\ell 0, \nu}]$ and the inverse $\hat{\mathbf{C}}_\ell^{-1}$ of the matrix $\hat{\mathbf{C}}_\ell \equiv [C_{\ell, \nu_1 \nu_2}]$.

In terms of spherical harmonic expansion coefficients, constraint (i) reads

$$\sum_\nu \sum_{\ell=0}^\infty f_\nu \tau_{\ell 0, \nu} \psi_{\ell 0, \nu} = \sum_{\ell=0}^\infty \mathbf{F}_\ell \psi_\ell = 1. \tag{45}$$

Performing functional variation (with respect to the filter function ψ_ℓ) of $\sigma_u^2(R_1, \ldots, R_N)$ while incorporating the (isoperimetric) boundary condition (45) through a Lagrangian multiplier yields the spherical matched filter ψ_ℓ

$$\psi_\ell = \alpha\, \hat{\mathbf{C}}_\ell^{-1} \mathbf{F}_\ell, \quad \text{where} \quad \alpha^{-1} = \sum_{\ell=0}^\infty \mathbf{F}_\ell^{\mathrm{T}} \hat{\mathbf{C}}_\ell^{-1} \mathbf{F}_\ell. \tag{46}$$

In any realistic application, the cross-power spectrum $C_{\ell, \nu_1 \nu_2}$ can be computed from observed data provided the cross-power spectrum of the signal is negligible. The quantities α, $\mathbf{F}_{\ell 0}$ and thus $\psi_{\ell 0}$ can be computed in a straightforward manner for a specific frequency dependence f_ν and for a model source profile $\tau_\nu(\theta)$.

6.4 Scale-adaptive filter on the sphere

The scale-adaptive filter ψ_ℓ satisfying all three conditions is given by

$$\psi_\ell = \hat{\mathbf{C}}_\ell^{-1}(\alpha\, \mathbf{F}_\ell + \mathbf{G}_\ell), \quad \text{with } \mathbf{G}_\ell \equiv [\mu_{\ell,\nu}\, \beta_\nu] \text{ and} \tag{47}$$

$$\mu_{\ell,\nu} \equiv f_\nu \tau_{\ell 0, \nu} \left(2 + \frac{\mathrm{d}\ln \tau_{\ell 0, \nu}}{\mathrm{d}\ln \ell} \right) = f_\nu [2\tau_{\ell 0, \nu} + \ell(\tau_{\ell 0, \nu} - \tau_{\ell-1 0, \nu})]. \tag{48}$$

As motivated in Section A5, the logarithmic derivative of $\tau_{\ell 0}$ with respect to the multipole order ℓ is a shorthand notation of the differential quotient which is only valid for $\ell \gg 1$. The quantities α and β_ν are given by the components

$$\alpha = (\hat{\mathbf{A}}^{-1})_{00}, \qquad \beta_\nu = (\hat{\mathbf{A}}^{-1})_{\nu 0}, \tag{49}$$

where $\hat{\mathbf{A}}$ is the $(1 + N) \times (1 + N)$ matrix with elements

$$A_{00} \equiv \sum_{\ell=0}^\infty \mathbf{F}_\ell^{\mathrm{T}} \hat{\mathbf{C}}_\ell^{-1} \mathbf{F}_\ell, \qquad A_{0\nu} \equiv \sum_{\ell=0}^\infty \mu_{\ell,\nu} \left(\mathbf{F}_\ell^{\mathrm{T}} \hat{\mathbf{C}}_\ell^{-1} \right)_\nu, \tag{50}$$

$$A_{\nu 0} \equiv \sum_{\ell=0}^\infty \mu_{\ell,\nu} \left(\hat{\mathbf{C}}_\ell^{-1} \mathbf{F}_\ell \right)_\nu, \quad A_{\nu\nu'} \equiv \sum_{\ell=0}^\infty \mu_{\ell,\nu}\, \mu_{\ell,\nu'} \left(\hat{\mathbf{C}}_\ell^{-1} \right)_{\nu\nu'}. \tag{51}$$

In these equations, no summation over the indices is implied.

6.5 Detection level and gain

As described by Sanz et al. (2001), the concept of constructing an optimized filter function for source detection aims at maximizing the signal-to-noise ratio D_u,

$$D_u \equiv \frac{\langle u(R_1, \ldots, R_N; \mathbf{0}) \rangle}{\sigma_u(R_1, \ldots, R_N)} = A\, \frac{\sum_{\ell=0}^\infty \mathbf{F}_\ell \psi_\ell}{\sqrt{\sum_{\ell=0}^\infty \psi_\ell^{\mathrm{T}} \hat{\mathbf{C}}_\ell \psi_\ell}}. \tag{52}$$

Computing the dispersion of the unfiltered field on the sphere yields the signal-to-noise ratio D_s of a signal on the fluctuating background:

$$\sigma_s^2 = \sum_{\nu_1, \nu_2} \sum_{\ell=0}^\infty C_{\ell,\, \nu_1 \nu_2} \quad \Rightarrow \quad D_s = \frac{A}{\sigma_s}. \tag{53}$$

These considerations allow introducing the *gain* for comparing the signal-to-noise ratios of a peak before and after convolution with a filter function

$$g \equiv \frac{D_u}{D_s} = \frac{\sigma_s}{\sigma_u(R_1, \ldots, R_N)}. \tag{54}$$

If the noise suppression is successful, the gain g will assume values larger than one. If the filters are constructed efficiently, they are able to reduce the dispersion ($\sigma_u(R_1, \ldots, R_N) < \sigma_s$) while simultaneously retaining the expectation value of the field (42). Due to the additional third constraint, the scale-adaptive filter is expected to achieve smaller gains compared to the matched filter.

6.6 Numerical derivation of filter kernels

For the derivation of suitable filter kernels the source profiles are assumed to be generalized King profiles as described by equation (36) convolved with the respective *Planck* beam superimposed on fluctuating background given by template $\langle S_{\ell m} \rangle_\nu$ coefficients. The inversion of the matrix $\hat{\mathbf{C}}_\ell$ (cf. equations 32 and 37) can be performed using either Gauss–Jordan elimination or LU decomposition, which both were found to yield reliable results. In the derivation of the scale-adaptive filters, however, it is numerically advantageous to artificially exclude the lower multipoles $\ell \leqslant 1$ from the calculation. Due to the submillimetric emission of the Milky Way, the lower multipoles are very large. Consequently, the corresponding $\psi_{\ell m}$ coefficients, $\ell \leqslant 1$, have been set to zero, which is not a serious intervention since the filters are designed to amplify structures at angular scales well below a degree. For consistency, the multipoles below the quadrupole have been artificially removed in the derivation of the matched filters as well.

In contrast to the *Planck* simulation pipeline all numerical calculations presented here are carried out in terms of fluxes measured in Jy and not in antenna temperatures for the following reason: cross-power spectra $C_{\ell, \nu_1 \nu_2}$ given in terms of antenna temperatures are proportional to $(\nu_1 \nu_2)^{-2}$ which results in a suppression of the highest frequency channels by a factor of almost 10^5 compared to the lowest frequency channels.

Furthermore, by working with fluxes instead of antenna temperatures, the filters for extracting the SZ signal show frequency dependences which can be understood intuitively. The frequency dependence is described by equations (29) and (30). The normalization $\mathcal{Y}$ has been chosen to be 1 arcmin^2, which corresponds to the weakest signals *Planck* will be able to detect. Because of the smallness of the source profiles to be detected, the calculations were carried out to multipole orders of $\ell_{\max} = 4096$, which ensures that the beams as well as the source profiles are well described. In the plots in Section 6.7, the filters depicted are smoothed with a moving average window comprising eleven bins for better visualization.

6.7 Discussion of filter kernels

6.7.1 Matched filter

The spherical harmonics expansion coefficients $\psi_{\ell 0, \nu}$ following from the matched filter algorithm are depicted in Fig. 15 for four frequencies most relevant to SZ observations, namely for $\nu = 100$, 143, 217 and 353 GHz. As background noise components the clean COS data set (left-hand column) and the exhaustive GAL data set (right-hand column) are contrasted. The filter kernels have been derived for optimized detection of sources described by a generalized King
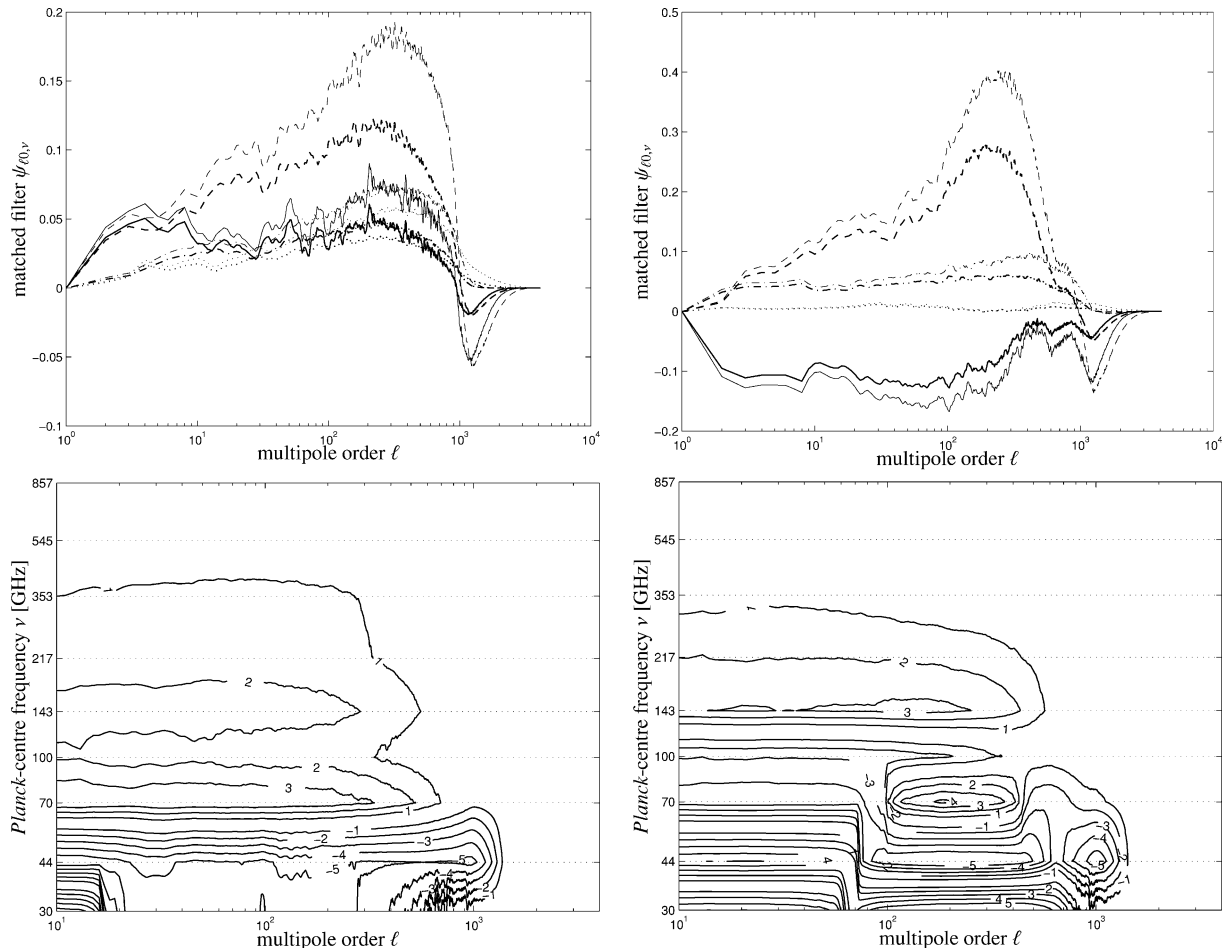
Figure 15. Upper panel: spherical harmonics coefficients $\psi_{\ell 0,\nu}$ as derived with the matched filter algorithm, for $\nu = 100$ GHz (solid line), $\nu = 143$ GHz (dashed line), $\nu = 217$ GHz (dash–dotted line) and $\nu = 353$ GHz (dotted line). The left- and right-hand columns compare filter kernels derived for a data set containing only the CMB, the SZ effects and instrumental noise (left-hand column) and for a data set comprising all Galactic foregrounds in addition (right-hand column). The filter kernels are optimized for the detection of generalized King profiles with core radii $\theta_c = 3.0$ arcmin (thin lines), $\theta_c = 5.0$ arcmin (thick lines) and asymptotic slope $\lambda = 1.0$. Lower panel: contour plot of the spherical harmonics expansion coefficients $\psi_{\ell 0,\nu}$ derived with the matched filter algorithm as a function of both the multipole moment order ℓ and *Planck*'s observing frequency ν. The filter kernels have been derived for an optimized detection of a generalized King profile with $(\theta_c, \lambda) = (15.0$ arcmin, 1.0). The contours are linearly spaced in arsinh ($10^2 \psi_{\ell 0,\nu}$).

profile with angular core radii $\theta_c = 3.0$ arcmin and $\theta_c = 5.0$ arcmin and asymptotic slope $\lambda = 1.0$.

The principle how the matched filter extracts the SZ signal from the maps is explained by Fig. 15. The SZ profiles the filter has been optimized are small structures at angular scales corresponding to multipole moments of $\ell \simeq 10^3$. In channels below $\nu = 217$ GHz, the clusters are observed in absorption and the fluxes are decreased. For that reason, the filters have negative amplitudes at small angular scales for these specific frequencies. At larger scales, the fluctuations are suppressed by linear combination of the various channels, while the filtering functions show very similar shapes. Optimizing the filters for detection of core radii of 5.0 arcmin instead of 3.0 arcmin result in a shift of the negative peak at $\ell \simeq 10^3$ to smaller multipole orders. Instrumental noise which is important at even higher multipoles is suppressed by the filter's exponential decline at high ℓ above $\ell \gtrsim 2000$. The unwanted CMB fluctuations and all Galactic contributions at scales larger than the cluster scale are suppressed by weightings with varying sign so that the foregrounds are subtracted at the stage of forming linear combinations of the $\langle S_{\ell m} \rangle_\nu$ coefficients.

Furthermore, the contours of the matched filter kernels are given in Fig. 15 as functions of both inverse angular scale ℓ and observing frequency ν for differing noise contributions. The figures compare filters derived for differing background noise compositions. The filters shown serve for the optimized detection of generalized King profiles with core radius $\theta_c = 15.0$ arcmin and asymptotic slope $\lambda = 1.0$. These (rather large) values have been chosen for visualization purposes. For clarity, the contour denoting zero values has been omitted due to noisy data. In these figures it is apparent how the filters combine the frequency information in order to achieve a suppression of the unwanted foregrounds. At multipole moments of a few hundred, the filters exhibit changes in sign, such that the measurements at low frequencies are subtracted from the measurements at high frequencies in the linear combination of the filtered maps.

Fig. 16 illustrates the filter kernels $\psi_\nu(\theta)$ in real space for the same selection of frequencies and background noise components as given above. The filter kernels $\psi_\nu(\theta)$ have been synthesized from the $\psi_{\ell 0,\nu}$ coefficients using the alm2grid utility of the *Planck* simulation package. Here, the parameters of the King profile to be detected are $(\theta_c, \lambda) = (5.0$ arcmin, 1.0). The filter kernels are similar in shape
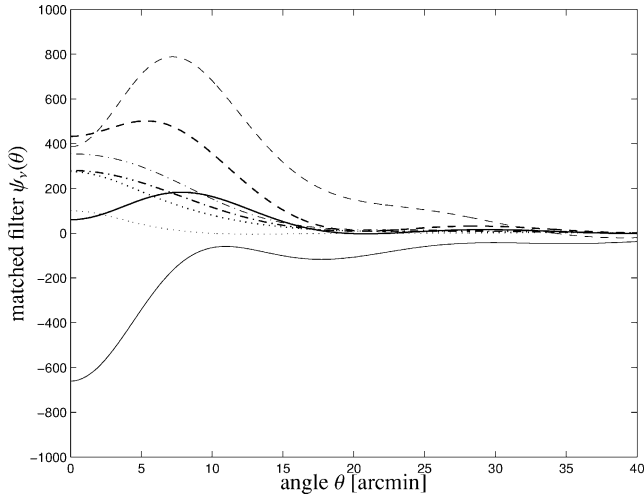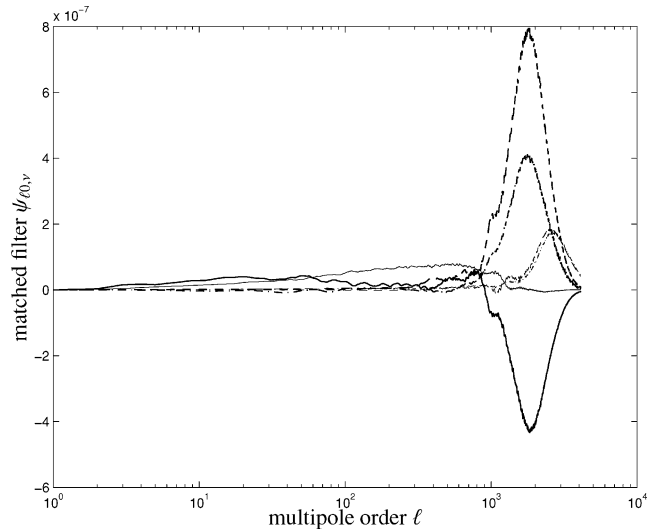
Figure 16. Matched filter kernels $\psi_\nu(\theta)$ in real space at SZ frequencies, i.e. for $\nu = 100$ GHz (solid line), $\nu = 143$ GHz (dashed line), $\nu = 217$ GHz (dotted line) and $\nu = 353$ GHz (dash–dotted line), for a data set including the CMB, Galactic foregrounds and instrumental noise (thin lines) and for a data set containing all Galactic components in addition to the CMB and instrumental noise (thick lines). The filter kernel is optimized for the detection of a generalized King profile with core radius $\theta_c = 5.0$ arcmin and asymptotic slope $\lambda = 1.0$.

Figure 17. Comparison of filter kernel $\psi_{\ell 0,\nu}$ coefficients derived for differing spectral dependences of the signal: thermal SZ effect (solid line), kinetic SZ effect (dashed line) and a Planckian emitter with surface temperature of $T_{surface} = 150$ K (dash–dotted line). All sources are assumed to be point-like, i.e. they appear to have the shape of the *Planck* beam. The curves are given for observing frequencies of $\nu = 143$ GHz (thin line) and $\nu = 217$ GHz (thick line) and have been derived with the matched filter algorithm. The noise is a composite of CMB fluctuations, Galactic and ecliptic foregrounds and instrumental noise.

to Mexican-hat wavelets, but show more than one oscillation. Their action on the sky maps is to apply high-pass filtering, such that all long-wavelength modes are eliminated. At the cluster scale, they implement a linear combination of the sky maps that aims at amplifying the SZ signal. The kernels derived for both the $\nu = 100$ and 143 GHz channels exhibit a central depression which is used to convert the SZ signal to positive amplitudes. The other two channels resemble simple Gaussian kernels which smooth the maps to a common effective angular resolution. At frequencies of $\nu = 217$ and 353 GHz the most important emission feature is Galactic Dust, which is suppressed by the filter's small amplitudes. In this way, the weak SZ signal is dissected.

In Fig. 17, filter kernels derived with both algorithms for point sources (i.e. with beam profiles of the respective *Planck* channels) are compared, that have been optimized for the detection of varying spectral behaviour of the signal, in this case the thermal SZ effect, the kinetic SZ effect and a Planckian thermal emitter with a surface temperature $T_{surface}$ of 150 K, such as an asteroid or planet. The filter kernels depicted correspond to observing frequencies of $\nu = 143$ and 217 GHz. The filters clearly reflect the spectral behaviour of the emission laws of the sources one aims at detecting: while the filter kernels designed for detecting thermal SZ clusters reflect the peculiar change in sign in the frequency dependence of the SZ effect, the other two curves show the behaviour to be expected for a Planckian emitter and the kinetic SZ effect, respectively. Again, the better angular resolution of the $\nu = 217$ GHz channel is apparent by the shifting of the curves to higher multipole order ℓ.

6.7.2 Scale-adaptive filter

The spherical harmonics expansion coefficients $\psi_{\ell 0,\nu}$ following from the scale-adaptive filter algorithm for the frequencies $\nu = 100$, 143, 217 and 353 GHz are given in the upper panel of Fig. 18. The left- and right-hand columns compare the filter kernels for differing noise components. Their functional shape has a number of impor-

tant features in common with the matched filters: they suppress the uncorrelated pixel noise, which is dominant at high ℓ by their exponential decline at $\ell \gtrsim 2000$. Furthermore, the filters amplify the SZ signal, which is negative at frequencies below $\nu = 217$ GHz, by assuming large negative values and hence converting the SZ signal to yield positive amplitudes. Additionally, the filters show a distinct secondary peak at $\ell \simeq 2000$ which causes the kernels to be more compact after transformation to real space and enables the size measurement. A more general observation is that the scale-adaptive filter kernel shapes are more complex and noisier in comparison to the matched filter, especially at high ℓ.

The scale-adaptive filter makes even stronger use of the spectral information than the matched filter. Especially the contour plots in Fig. 18 show that the scale-adaptive filter exhibits alternating signs when varying the observing frequency ν while keeping the angular scale ℓ fixed. In this way, the noise contributions are isolated in angular scale and subsequently suppressed by linear combination of the maps. Furthermore, one notices a change in sign at multipole order $\ell \simeq 200$ which is common to the frequencies $\nu = 100$–353 GHz, at which the CMB signal is strongest. Aiming at reducing the variance of the filtered maps, the scale-adaptive filter is suppressing the $\langle S_{\ell m}\rangle_\nu$ coefficients by assuming small values.

Fig. 19 gives the filter kernels $\psi_\nu(\theta)$ in real space for selected frequencies and background noise components. The scale-adaptive filters work similarly as the matched filters like Mexican-hat wavelets and subject the sky maps to high pass filtering.

In Fig. 20, filter kernels derived with both algorithms for point sources (i.e. with beam profiles of the respective *Planck* channels) are compared, that have been optimized for the detection of varying spectral behaviour of the signal, in this case the thermal SZ effect, the kinetic SZ effect and a Planckian thermal emitter with a surface temperature $T_{surface}$ of 150 K, such as an asteroid or planet. The filter kernels depicted correspond to observing frequencies of $\nu = 143$
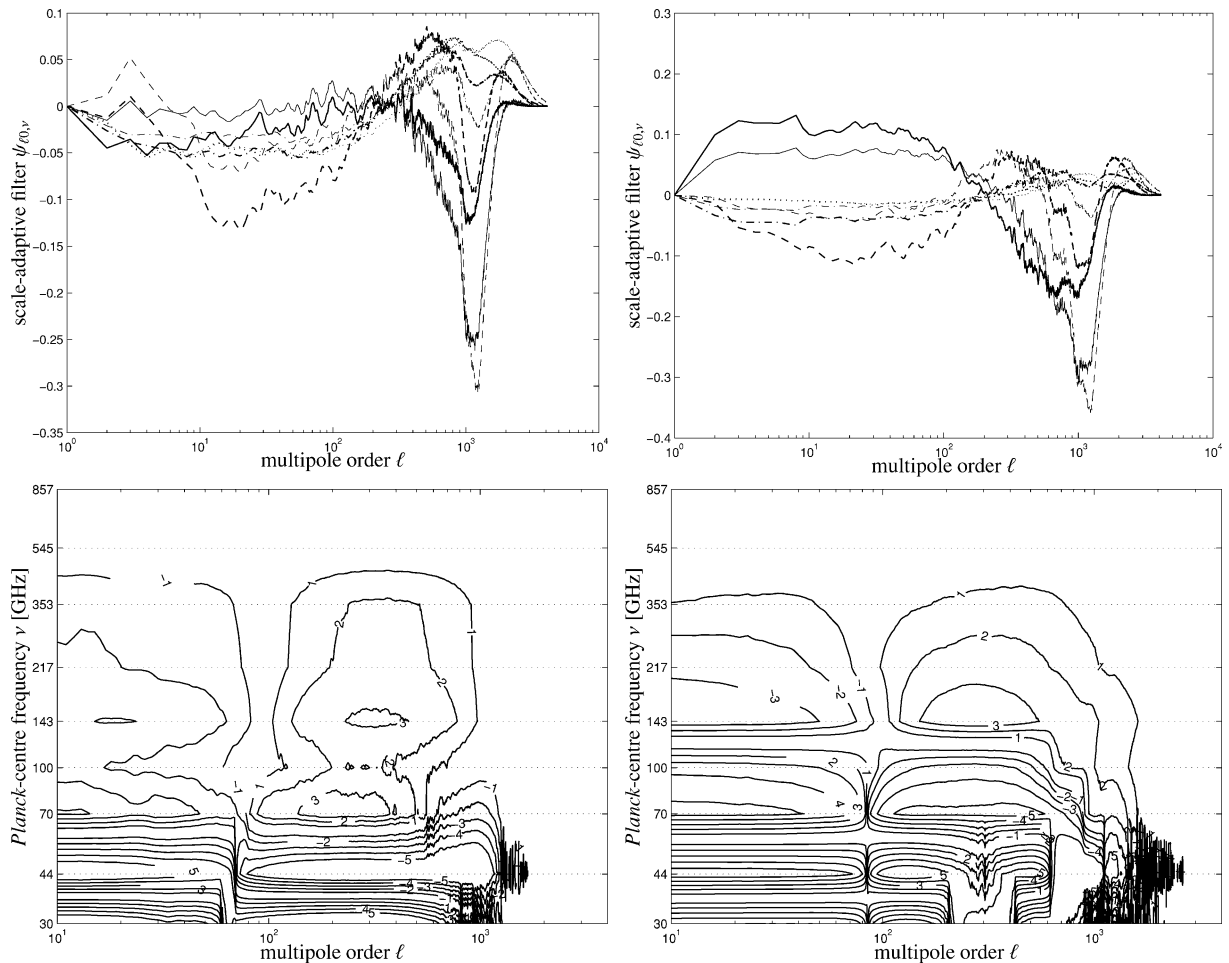
Figure 18. Upper panel: spherical harmonics coefficients $\psi_{\ell 0,\nu}$ as derived with the scale-adaptive filter algorithm, for $\nu = 100\,\mathrm{GHz}$ (solid line), $\nu = 143\,\mathrm{GHz}$ (dashed line), $\nu = 217\,\mathrm{GHz}$ (dash–dotted line) and $\nu = 353\,\mathrm{GHz}$ (dotted line). The filter kernel is optimized for the detection of generalized King profiles with core radii $\theta_c = 3.0\,\mathrm{arcmin}$ (thin lines) and $\theta_c = 5.0\,\mathrm{arcmin}$ (thick lines) and asymptotic slope $\lambda = 1.0$. Lower panel: contour plots of the spherical harmonics expansion coefficients $\psi_{\ell 0,\nu}$ derived with the scale-adaptive filter algorithm as a function of both the multipole moment order ℓ and *Planck*'s observing frequency ν are shown. The filter kernels have been derived for an optimized detection of a generalized King profile with $(\theta_c, \lambda) = (15.0\,\mathrm{arcmin}, 1.0)$. The contours are linearly spaced in $\mathrm{arsinh}\,(10^2\psi_{\ell 0,\nu})$. Again, the columns compare the influence of the fluctuating background, comprising cosmological contributions (CMB and both SZ effects) and instrumental noise (left-hand column) to the data set that contains all Galactic foregrounds in addition.

and 217 GHz. As in the case of the matched filter, the frequency dependence of the signal is reflected by the sign of the filter kernel at the anticipated angular scale of the profile to be detected.

6.7.3 *Influence of point sources on the filter construction*

Microwave point sources, as discussed in Section 4.7, constitute a contribution to the noise spectrum at high multipoles ℓ. In fact, for randomly positioned point sources, one expects a power-law angular power spectrum with an exponent close to 2. This section aims to investigate how point sources, which have been omitted from the analysis, interfere with the filter construction.

In general, enhanced levels of noise shift the peak of the filter functions to larger angular scales, so that the peak of the sources one aims to amplify are dispersed over a larger area. Consequently, the central peak value drops, as the normalization is conserved in the convolution process. Hence, stronger noise levels result in smaller gain factors after filtering, even for optimized filters.

In order to investigate quantitatively to which extent the inclusion of point sources affects the efficiency of the filtering algorithms, we

consider a simplified toy model that should capture the essential physics. Here, a circularly symmetric source profile $\tau(\theta)$ is superimposed on a fluctuating background, whose fluctuation statistics is described by the angular power spectrum $C(\ell)$. For illustrative purposes, the derivation is restricted to matched filtering of a single-frequency observation, and the computation is carried out on a plane tangential to the celestial sphere, where the small-angle approximation is valid.
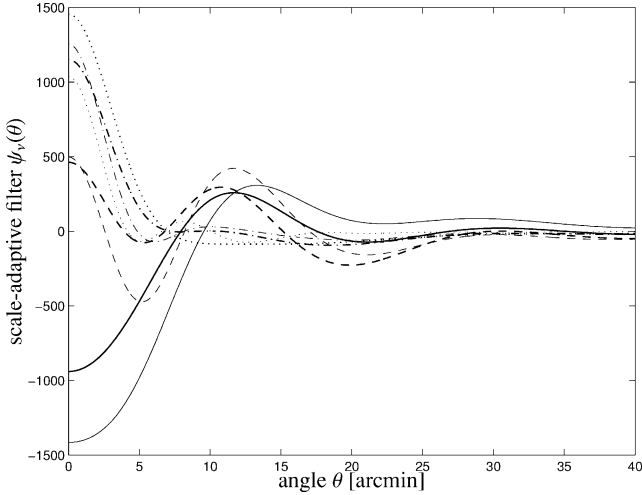
For simplicity, a Gaussian source profile $\tau(\theta)$ is chosen, for which the Fourier transform can be readily determined:

$$\tau(\theta) = \frac{1}{2\pi\theta_c^2}\exp\left(-\frac{\theta^2}{2\theta_c^2}\right) \rightarrow \tau(\ell) = \int\frac{\mathrm{d}^2\theta}{(2\pi)^2}\tau(\theta)\exp(\mathrm{i}\boldsymbol{\ell\theta}).$$

(55)

Carrying out the transform yields

$$\tau(\ell) = \int\frac{\theta\,\mathrm{d}\theta}{2\pi}\tau(\theta)J_0(\ell\theta) = \frac{\exp\left(-2\theta_c^2\ell^2\right)}{4\pi^2}.$$

(56)

The noise model combines uncorrelated (instrumental) pixel noise, for which $C(\ell) \propto \ell^2$ with a second noise contribution due to point

Figure 19. Scale-adaptive filter kernels $\psi_\nu(\theta)$ in real space, for $\nu = 100$ GHz (solid line), $\nu = 143$ GHz (dashed line), $\nu = 217$ GHz (dotted line) and $\nu = 353$ GHz (dash–dotted line), for a data set incorporating the CMB, Galactic foregrounds and instrumental noise. The filter kernel is optimized for the detection of a generalized King profile with parameters $(\theta_c, \lambda) = (5.0 \text{ arcmin}, 1.0)$.
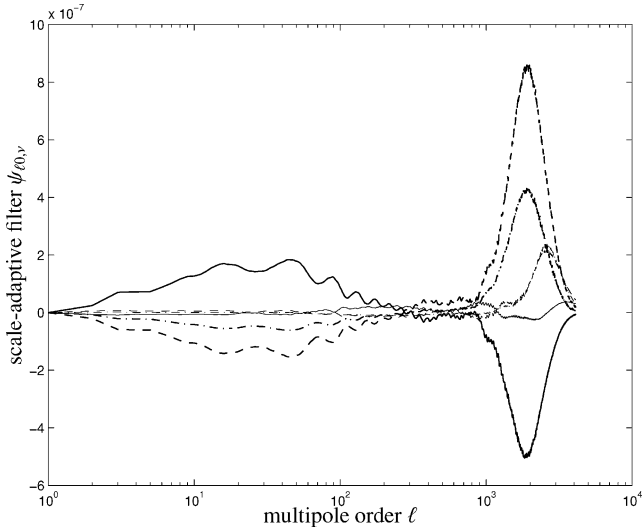

Figure 20. Comparison of filter kernel $\psi_{\ell 0, \nu}$ coefficients derived for differing spectral dependences of the signal: thermal SZ effect (solid line), kinetic SZ effect (dashed line) and a Planckian emitter with surface temperature of $T_{\text{surface}} = 150$ K (dash–dotted line). All sources are assumed to be point-like, i.e. they appear to have the shape as the *Planck* beam. The curves are given for observing frequencies of $\nu = 143$ GHz (thin line) and $\nu = 217$ GHz (thick line) and have been derived with the scale-adaptive filter algorithm. The noise is a composite of CMB fluctuations, Galactic and ecliptic foregrounds and instrumental noise.

sources, parametrized by $C(\ell) \propto \ell^\alpha$. The variable q adjusts the relative normalization of the noise models and the exponent α is left as a free parameter in order to include deviations from a pure Poissonian process:

$$C(\ell) = \ell(\ell + 1) + q\ell^\alpha \simeq \ell^2 + q\ell^\alpha. \tag{57}$$

For a single-frequency observation, the Fourier-transformed matched filter $\psi(\ell)$ is defined by
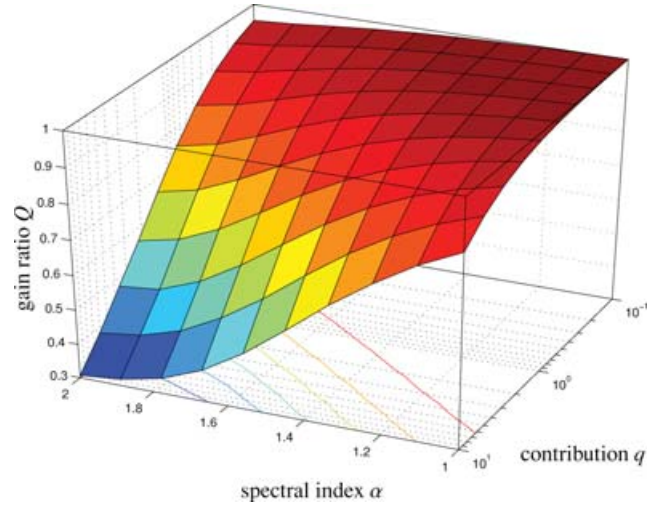
Figure 21. Normalized gain factor $Q \equiv D_u/D_s$ for a noise model combining instrumental noise and point sources, as a function of power-law index α and amplitude q of the point-source angular power spectrum.

$$\psi(\ell) = \left[\int \ell \mathrm{d}\ell \frac{\tau^2(\ell)}{C(\ell)} \right]^{-1} \frac{\tau(\ell)}{C(\ell)}. \tag{58}$$

The signal-to-noise ratio of a peak before filtering can be determined from

$$D_s = \frac{\int \ell \mathrm{d}\ell \tau(\ell)}{\sqrt{\int \ell \mathrm{d}\ell C(\ell)}}, \tag{59}$$

whereas the signal-to-noise ratio after filtering is given by

$$D_u = \frac{\int \ell \mathrm{d}\ell \psi(\ell)\tau(\ell)}{\sqrt{\int \ell \mathrm{d}\ell \psi^2(\ell)C(\ell)}}. \tag{60}$$

The gain ratio Q can be determined from the signal-to-noise ratios:

$$Q = \frac{D_u}{D_s}, \tag{61}$$

and is a function of the source core radius θ_c, of the parameters α and q of the noise model and of the range of multipole moments considered, due to the absence of a cut-off scale in $C(\ell)$.

The results are shown in Fig. 21, where Q is normalized to the value 1 for a noise spectrum with negligible point-source contribution. Concerning the relative normalization q of the two noise contributions, values ranging from $q = 0.1$ (weak point-source contribution to $C(\ell)$) to $q = 10$ are considered (dominating point-source noise). Spectral indices α in the physically interesting range α were examined. The core size θ_c of the source profile was set to 10.0 arcmin. Fig. 21 suggests, that the gain is sensitive to strong admixture of point sources to the noise power spectrum for steep spectral indices α, as expected from the qualitative discussion at the beginning of the section.

For a realistic value of $\alpha = 2$, a point-source contribution of 30 per cent to the noise power spectrum results in a 10 per cent drop in filter efficiency. If the point-source contribution is of equal magnitude as the pixel noise, the filter efficiency can be expected to decrease as much as 30 per cent.

6.8 Filter renormalization and synthesis of likelihood maps

Once the filter kernels are derived, the filtered fields $u_\nu(R_\nu, \beta)$ can be synthesized from the $u_{\ell m, \nu}$ coefficients (defined in equation 40)

and the resulting maps can be added in order to yield the co-added, filtered field $u(R_1, \ldots, R_N, \beta)$ (see equation 41), which can be normalized by the level of fluctuation σ_u (given by equation 42) to yield the likelihood map $D(\theta)$. It is favourable to divide the filter kernels by the variance σ_u and to apply a renormalization:

$$\psi_{\ell 0, \nu} \longrightarrow \psi'_{\ell 0, \nu} = \frac{\psi_{\ell 0, \nu}}{\sqrt{\sum_\ell \psi_\ell^{\mathrm{T}} \hat{\mathbf{C}}_\ell \psi_\ell}}. \tag{62}$$

In this case, the filter kernels are invariant under changes in profile normalization. With these kernels, the filtered flux maps can be synthesized from the set of $\langle S_{\ell m} \rangle_\nu$ coefficients and the resulting maps can be co-added to yield the final normalized likelihood map $D(\beta)$. It is computationally advantageous, however, to interchange the last two steps,

$$D_u(\boldsymbol{\beta}) = \frac{u(\boldsymbol{\beta})}{\sigma_u} = \frac{1}{\sigma_u} \sum_\nu u_\nu(\boldsymbol{\beta}), \tag{63}$$

$$= \sum_\nu \sum_{\ell=0}^\infty \sum_{m=-\ell}^{+\ell} \sqrt{\frac{4\pi}{2\ell+1}} \langle S_{\ell m} \rangle_\nu \frac{\psi_{\ell 0, \nu}}{\sqrt{\sum_\ell \psi_\ell^{\mathrm{T}} \hat{\mathbf{C}}_\ell \psi_\ell}} Y_\ell^m(\boldsymbol{\beta}), \tag{64}$$

$$= \sum_{\ell=0}^\infty \sum_{m=-\ell}^{+\ell} \sqrt{\frac{4\pi}{2\ell+1}} \underbrace{\left[\sum_\nu \langle S_{\ell m} \rangle_\nu \, \psi'_{\ell 0, \nu} \right]}_{\equiv D_{\ell m}} Y_\ell^m(\boldsymbol{\beta}), \tag{65}$$

and to derive the $D_{\ell m}$ coefficients first, such that the synthesis has to be performed only once. Due to the restriction to axially symmetric kernels, the convolution can be carried out using the alm2map utility rather than totalconvolve.

Fig. 22 gives a visual impression of the capability of the above-described filtering schemes. The figure shows a 30×30-deg^2 wide field at the ecliptic North pole at a frequency of $\nu = 353$ GHz (at the SZ maximum) as observed by *Planck*, i.e. the image is smoothed to an angular resolution of $\Delta\theta = 5.0$ arcmin (FWHM) and contains the fluctuating CMB, all Galactic and ecliptic foregrounds as well as pixel noise. Matched and scale-adaptive filter kernels were derived for isolating point sources, i.e. for sources that appear to have profiles equal to *Planck*'s beams of the corresponding channel. For clarity, only amplitudes exceeding a threshold value of 1.0σ are shown.

For comparison, Fig. 22 shows the same detail of the input thermal SZ map as well. It is immediately apparent that the observation of SZ clusters without foreground and noise suppression is not possible and that one has to rely on filtering schemes. As a comparison with Fig. 22 shows, the filters are clearly able to isolate the SZ clusters and to strongly suppress all spurious noise contributions. The matched filter, however, shows a slightly better performance and yields more significant peaks due to better background suppression. There are weak residuals present in both maps due to incomplete foreground reduction. These residuals however, have small amplitudes compared to the SZ detections. The highest peaks exhibit detection significances amounting to 10.6σ in the case of the matched filter and 9.1σ in the case of the scale-adaptive filter.

It should be emphasized that the filters work exceptionally well despite the fact that the Milky Way clearly is a non-Gaussian feature, whereas Gaussianity of the fluctuating background was an important assumption in the derivation of the filter kernels. Furthermore, the filters successfully separate and amplify the weak SZ signal in the

presence of seven different noise contributions (CMB, four Galactic foregrounds, thermal emission from bodies of the Solar system and instrumental noise) that exhibit different spectral behaviours by relying on just nine broad-band measurements. Fig. 23 summarizes all steps involved in the simulation of *Planck* observations, filter derivation and signal extraction.

7 SUMMARY AND CONCLUSION

A simulation for assessing *Planck*'s SZ capabilities in the presence of spurious signals is presented that combines maps of the thermal and kinetic SZ effects with a realization of the CMB, in addition to Galactic foregrounds (synchrotron emission, free–free emission, thermal emission from dust, CO-line radiation) as well as the sub-millimetric emission from celestial bodies of our Solar system. Additionally, observational issues such as the finite angular resolution and spatially non-uniform instrumental noise of *Planck* are taken into account.

(i) Templates for modelling the free–free emission and the CO-line emission have been added to the *Planck* simulation pipeline. The free–free template relies on an Hα survey of the Milky Way. The spectral properties of both foregrounds are modelled with reasonable parameter choices, i.e. $T_{\mathrm{p}} = 10^4$ K for the free–free plasma temperature and $T_{\mathrm{CO}} = 20$ K for the mean temperature of GMCs.

(ii) An extensive package for modelling the submillimetric emission from planet and asteroids has been implemented for *Planck*, that solves the heat balance equation of each celestial body. It takes the movement of the planets and asteroids into account, which causes, due to *Planck*'s scanning strategy, double detections separated by approximate half-year intervals. The total number of asteroids implemented is $\simeq 1200$.

(iii) The foregrounds have been combined under proper inclusion of *Planck*'s frequency response windows in order to yield a set of flux maps. The autocorrelation and cross-correlation properties of those maps are investigated in detail. Furthermore, their decomposition into spherical harmonics $\langle S_{\ell m} \rangle_\nu$ serve as the basis for the filter construction. It should be emphasized that the spectral properties of a foreground component were assumed to be isotropic.

(iv) In order to separate the SZ Signal and to suppress the foreground components, the theory of matched and scale-adaptive filtering has been extended to spherical data sets. The formulae in the context of spherical coordinates and Y_ℓ^m decomposition are analogous to those derived for Cartesian coordinate systems and Fourier transforms.

(v) The global properties of filter kernel shapes are examined as functions of observing channel, composition of noise, parameters of the profile to be detected and spectral dependence of the signal. Transformation of the filter kernels to real space yields functions that resemble the Mexican-hat wavelets, but show more than one oscillation. The shape of the filter kernels can be understood intuitively: they subject the maps to high-pass filtering while retaining structures similar in angular extent to the predefined profile size. The signal is then amplified by linear combination of the maps, which again is apparent in the sign of the filter kernels.

(vi) The functionality of the filtering scheme is verified by applying them to simulated observations. It is found that the Galactic foregrounds can be suppressed very effectively so that the SZ cluster signals can be retrieved. Comparing the two filters, the scale-adaptive filter performs not as good as the matched filter, which
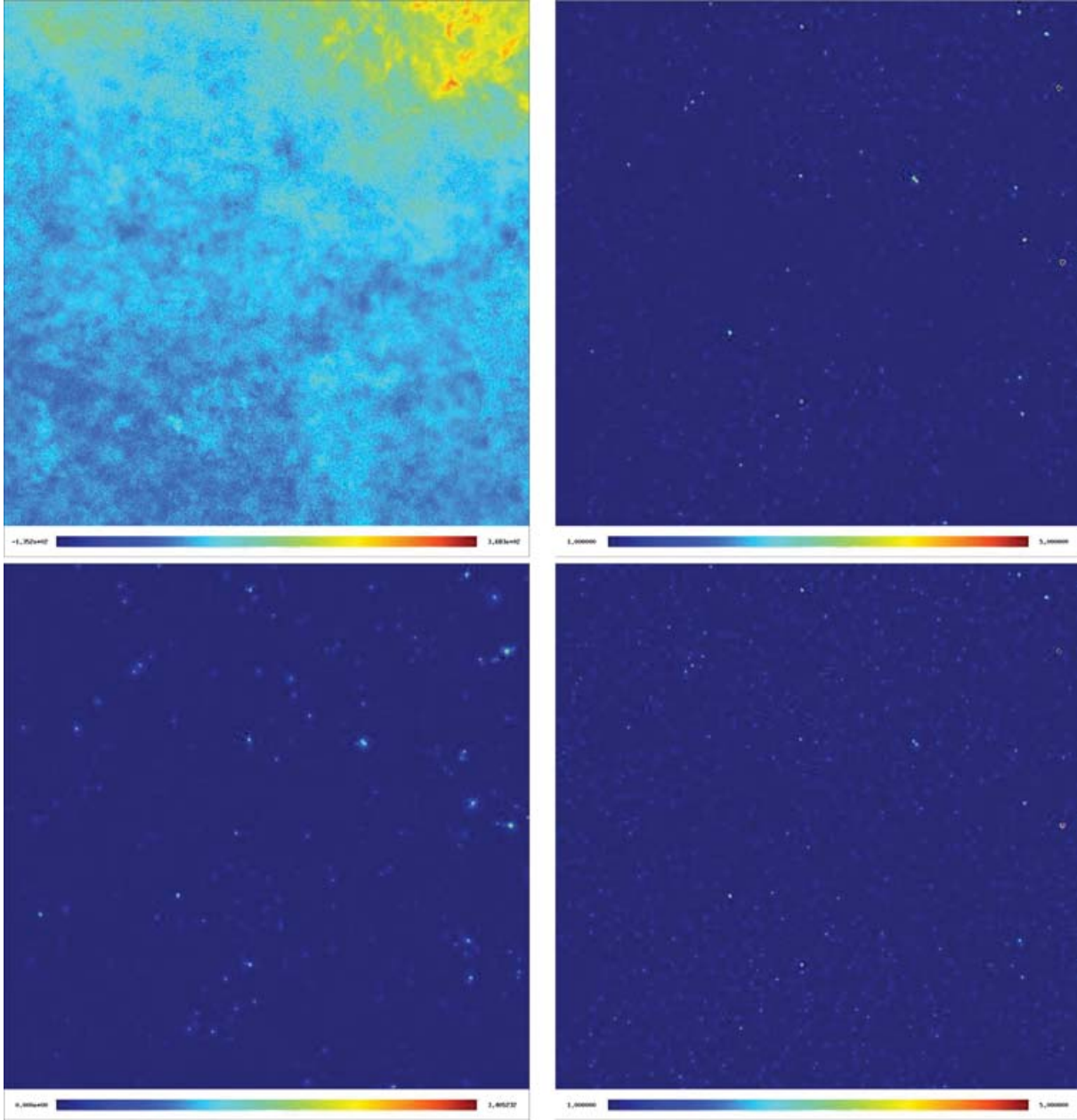
Figure 22. Upper left-hand panel: a 30×30-deg^2 wide field centred on the ecliptic North pole as synthesized from a data set containing the CMB, all Galactic and ecliptic foregrounds and instrumental noise for an observing frequency of $\nu = 353$ GHz is shown. The amplitudes are proportional to arsinh ($T_A(\nu = 353$ GHz) μK^{-1}) and the field is smoothed with the corresponding *Planck* beam of $\Delta\theta = 5.0$ arcmin (FWHM). Upper right-hand panel: the same field is shown after reconstruction from the $D_{\ell m}$ coefficients. Here, filters derived with the matched filter algorithm optimized for detecting point sources were employed. The amplitudes are given in detection significances and the shading scales linearly. Lower right-hand panel: again, the same field is shown after synthesis from the $D_{\ell m}$ coefficients but in this case, filters derived with the scale-adaptive filter algorithm optimized for detecting point sources were used. The amplitudes are stated as detection significances in units of σ and the shading is linear. In the lower left-hand panel, the corresponding field taken from the original thermal SZ map is given for comparison. The amplitudes are $\propto$ arsinh(10^4y).

is in accordance to the findings of Herranz et al. (2002a,b). It should be emphasized that for the derivation of the filter kernels nothing but a model profile and all cross-power spectra (in *Planck*'s case a total number of 45 independent $C_{\ell,\nu_1\nu_2}$ sets) are used.

The scientific exploitation of our simulation and the characterization of *Planck*'s SZ cluster sample, e.g. the number density as a function of detection significance as well as filter parameters, spatial

homogeneity of the cluster sample and the population of the detections in the mass–redshift plane will be the subject of a forthcoming paper.
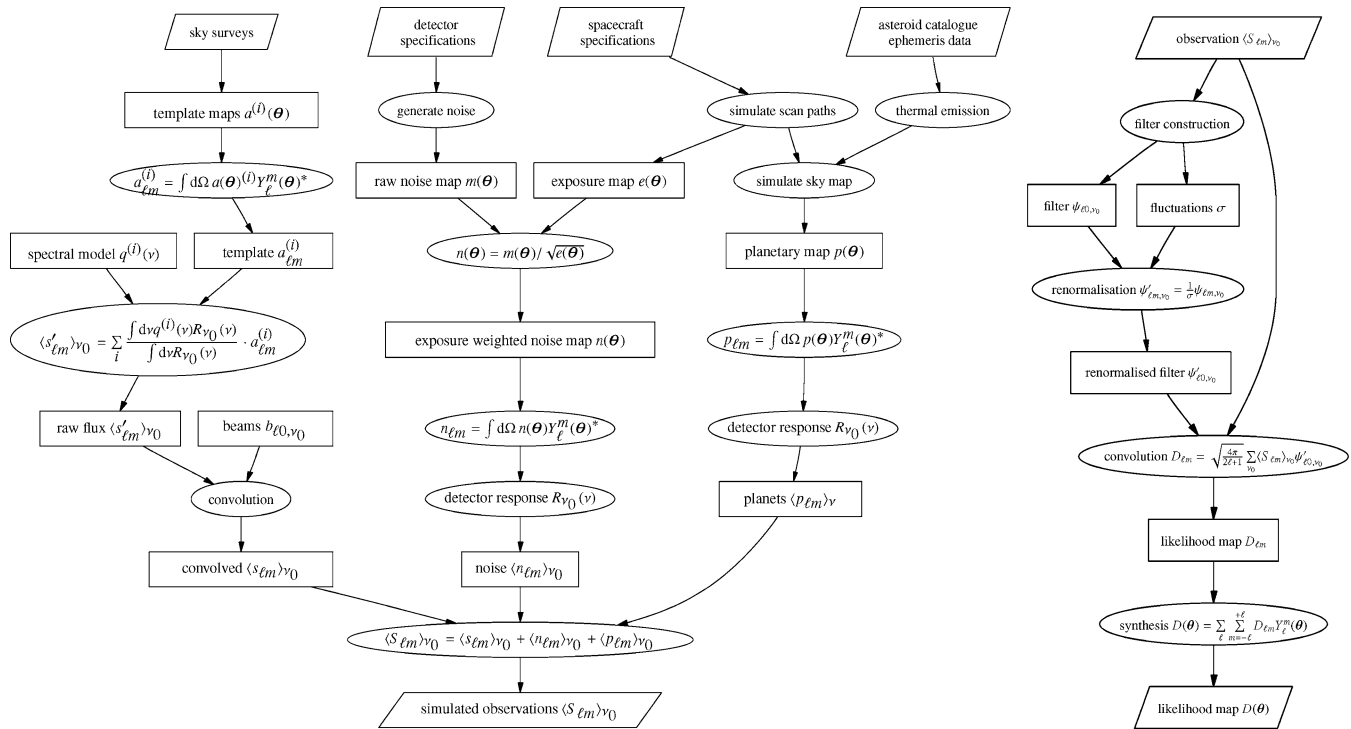
Figure 23. Flow chart summarizing all steps involved in the simulation of *Planck* observations and the derivation of $\langle S_{\ell m}\rangle_\nu$ coefficients (left-hand panel) and in the filter construction and signal extraction (right-hand panel).

REFERENCES

Aghanim N., de Luca A., Bouchet F. R., Gispert R., Puget J. L., 1997, A&A, 325, 9
Aghanim N., Hansen S. H., Lagache G., 2005, A&A, 439, 901
Arfken G. B., Weber H. J., 1995, Mathematical Methods for Physicists. Academic Press, San Diego
Barbosa D., Bartlett J. G., Blanchard A., Oukbir J., 1996, A&A, 314, 13
Barbosa D., Bartlett J. G., Blanchard A., 2000, Astrophys. Lett. Commun., 37, 383
Bartelmann M., 2001, A&A, 370, 754
Bennett C. L. et al., 1994, ApJ, 434, 587
Bennett C. L., Halpern M., Hinshaw G. et al., 2003a, ApJS, 148, 1
Bennett C. L. et al., 2003b, ApJS, 148, 97
Bersanelli M., Mandolesi N., 2000, Astrophys. Lett. Commun., 37, 171
Birkinshaw M., 1999, Phys. Rep., 310, 98
Bouchet F. R., Gispert R., 1999, New Astron., 4, 443
Bouchet F. R., Prunet S., Sethi S. K., 1999, MNRAS, 302, 663
Cayón L. et al., 2000, MNRAS, 315, 757
Church S., Knox L., White M., 2003, ApJ, 582, L63
Colberg J. M. et al. (The Virgo Consortium), 2000, MNRAS, 319, 209
Cremonese G., Marzari F., Burigana C., Maris M., 2002, New Astron., 7, 483
Dame T. M., Hartmann D., Thaddeus P., 1996, BAAS, 28, 1362
Dame T. M., Hartmann D., Thaddeus P., 2001, ApJ, 547, 792
Dickinson C., Davies R. D., Davis R. J., 2003, MNRAS, 341, 369
Diego J. M., Vielva P., Martínez-González E., Silk J., Sanz J. L., 2002, MNRAS, 336, 1351

Doré O., Teyssier R., Bouchet F. R., Vibert D., Prunet S., 2001, A&A, 374, 358
Draine B. T., Lazarian A., 1998, ApJ, 508, 157
Finkbeiner D. P., 2003, ApJS, 146, 407
Finkbeiner D. P., Davis M., Schlegel D. J., 1999, ApJ, 524, 867
Finkbeiner D. P., Davis M., Schlegel D. J., 2000, ApJ, 544, 81
Geisbüsch J., Kneissl R., Hobson M., 2005, MNRAS, 360, 41
Giardino G., Banday A. J., Górski K. M., Bennett K., Jonas J. L., Tauber J., 2002, A&A, 387, 82
Goldin A. B. et al., 1997, ApJ, 488, L161
Griffin M. J., Ade P. A. R., Orton G. S., Robson E. I., Gear W. K., Nolt I. G., Radostitz J. V., 1986, Icarus, 65, 244
Haslam C. G. T., Klein U., Salter C. J., Stoffel H., Wilson W. E., Cleary M. N., Cooke D. J., Thomasson P., 1981, A&A, 100, 209
Haslam C. G. T., Stoffel H., Salter C. J., Wilson W. E., 1982, A&AS, 47, 1
Herranz D., Sanz J. L., Hobson M. P., Barreiro R. B., Diego J. M., Martinez-Gonzalez E., Lasenby A. N., 2002a, MNRAS, 336, 1057
Herranz D., Sanz J. L., Barreiro R. B., Martinez-Gonzalez E., 2002b, ApJ, 580, 610
Hivon E., Wandelt B. D., Gorski K. M., 1998, in Banday A. J., Sheth R. K., da Costa L. N., eds, Proc. MPA–ESO Cosmology Conf., Evolution of Large-Scale Structure: From Recombination to Garching. ESO, Garching, p. 43
Hobson M. P., Jones A. W., Lasenby A. N., Bouchet F. R., 1998, MNRAS, 300, 1
Hobson M. P., Barreiro R. B., Toffolatti L., Lasenby A. N., Sanz J., Jones A. W., Bouchet F. R., 1999, MNRAS, 306, 232
Jenkins A., Frenk C. S., White S. D. M., Colberg J. M., Cole S., Evrard A. E., Couchman H. M. P., Yoshida N., 2001, MNRAS, 321, 372
Lagache G., 2003, A&A, 405, 813
Lagache G., Puget J. L., 2000, A&A, 355, 17
Lagerros J. S. V., 1996a, A&A, 310, 1011
Lagerros J. S. V., 1996b, A&A, 315, 625
Lagerros J. S. V., 1997, A&A, 325, 1226
Lagerros J. S. V., 1998, A&A, 332, 1123
Lamarre J. M., Puget J. L., Bouchet F., 2003, New Astron. Rev., 47, 1017

Leinert C., Ábrahám P., Acosta-Pulido J., Lemke D., Siebenmorgen R., 2002, A&A, 393, 1073

Maino D. et al., 1999, A&AS, 140, 383

Maino D. et al., 2002, MNRAS, 334, 53

Maris M., Burigana C., Fogliani S., 2006, A&A, 452, 685

Mather J. C., Fixsen D. J., Shafer R. A., Mosier C., Wilkinson D. T., 1999, ApJ, 512, 511

Moore P., 2000, The Data Book of Astronomy. IOP Publishing, Bristol, p. 529

Müller T. G., 2001, Planet. Space Sci., 49, 787

Müller T. G., Lagerros J. S. V., 1998, A&A, 338, 340

Müller T. G., Lagerros J. S. V., 1999, AAS/Division Planet. Sci. Meeting, 31

Müller T. G., Lagerros J. S. V., 2002, A&A, 381, 324

Natoli P., de Gasperis G., Gheller C., Vittorio N., 2001, A&A, 372, 346

Neugebauer G., Miinch G., Kieffer H., Chase S. C., Miner E., 1971, AJ, 76, 719

Puget J.-L., Abergel A., Bernard J.-P., Boulanger F., Burton W. B., Desert F.-X., Hartmann D., 1996, A&A, 308, L5

Reach W. T., Morris P., Boulanger F., Okumura K., 2003, Icarus, 164, 384

Rephaeli Y., 1995, ARA&A, 33, 541

Sanz J. L., Herranz D., Martínez-Gónzalez E., 2001, ApJ, 552, 484

Schäfer B. M., Pfrommer C., Bartelmann M., Springel V., Hernquist L., 2006, MNRAS, in press (doi: 10.1111/j.1365-2966.2006.10552.x) (astro-ph/0407089)

Schlegel D. J., Finkbeiner D. P., Davis M., 1997, Bull. Am. Astron. Soc., 29, 1354

Schlegel D. J., Finkbeiner D. P., Davis M., 1998, ApJ, 500, 525

Seljak U., Zaldarriaga M., 1996, ApJ, 469, 437

Sokasian A., Gawiser E., Smoot G. F., 2001, ApJ, 562, 88

Song Y., Cooray A., Knox L., Zaldarriaga M., 2003, ApJ, 590, 664

Spergel D. N. et al., 2003, ApJS, 148, 175

Springel V., Hernquist L., 2002, MNRAS, 333, 649

Springel V., Yoshida N., White S. D. M., 2001, New Astron., 6, 79

Stolyarov V., Hobson M. P., Ashdown M. A. J., Lasenby A. N., 2002, MNRAS, 336, 97

Sunyaev R. A., Zel'dovich I. B., 1972, Comments Astrophys. Space Phys., 4, 173

Sunyaev R. A., Zel'dovich I. B., 1980, ARA&A, 18, 537

Tegmark M., de Oliveira-Costa A., 1998, ApJ, 500, L83

Tegmark M., Efstathiou G., 1996, MNRAS, 281, 1297

Toffolatti L., Argueso Gomez F., de Zotti G., Mazzei P., Franceschini A., Danese L., Burigana C., 1998, MNRAS, 297, 117

Unsöld A., Baschek B., 2002, Der Neue Kosmos. Einführung in die Astronomie und Astrophysik. Springer-Verlag, Berlin

Valls-Gabaud D., 1998, PASA, 15, 111

Vielva P., Martínez-González E., Cayón L., Diego J. M., Sanz J. L., Toffolatti L., 2001a, MNRAS, 326, 181

Vielva P., Barreiro R. B., Hobson M. P., Martínez-González E., Lasenby A. N., Sanz J. L., Toffolatti L., 2001b, MNRAS, 328, 1

Villa F., Sandri M., Bersanelli M., Butler R. C., Mandolesi N., Mennella A., Marti-Canales J., Tauber J., 2003, in Proc. 25th Antenna Workshop on Satellite Antenna Technology. ESA-ESTEC (astro-ph/0304137)

Wandelt B. D., Górski K. M., 2001, Phys. Rev. D, 63, 123002

White M., 2003, ApJ, 597, 650

White M., Majumdar S., 2004, ApJ, 602, 565

White M., Hernquist L., Springel V., 2002, ApJ, 579, 16

Wright E. L., 1976, ApJ, 210, 250

Yvon D., Mayet F., 2005, A&A, 436, 729

APPENDIX A: OPTIMIZED FILTER FOR SINGLE FREQUENCY ALL-SKY OBSERVATIONS

This appendix derives the optimized filters for single frequency all-sky observations and thus serves as a detailed supplement to Section 6 where optimized filters for multifrequency observations were derived. The formalism outlined in this appendix might be applied to future all-sky surveys in the X-ray or microwave regime.

A1 Assumptions and definitions

In order to construct our filters, we consider an all-sky map of the detected scalar field $s(\theta)$:

$$s(\theta) = y(|\theta - \theta_0|) + n(\theta), \tag{A1}$$

where $\theta = (\vartheta, \varphi)$ denotes a two-dimensional vector on the sphere and θ_0 is the source location. The first term of the right-hand side represents the amplitude of the sources to be detected, while the second term in corresponds to the generalized noise present in the map which is composed of any detected features other than the desired signal including for instance instrumental noise. The statistical properties of the noise are assumed to be characterized by its power spectrum $\langle n_{\ell m} \, n_{\ell'm'}^* \rangle = C_\ell \, \delta_{\ell\ell'} \, \delta_{mm'}$. In order to sketch the construction of the optimized filter, we assume an individual cluster situated at the North pole ($\theta_0 = 0$) with a characteristic angular SZ signal $y(\theta = |\theta|) = A\tau(\theta)$, separating the amplitude A and the profile $\tau(\theta)$.

A2 Convolution theorem on the sphere

Filtering a scalar field on the sphere with an arbitrary, asymmetric kernel requires the specification of the convolution path as well as the orientation of the filter kernel at each position on the sphere in order to apply any convolution algorithm (Wandelt & Górski 2001). Because of the simplifying restriction to centrally symmetric filter kernels, we give the theorem for the convolution of two functions, one of which is assumed to be centrally symmetric. The filtered field $u(\beta)$ is obtained by convolution of the centrally symmetric filter function $\psi(\theta)$ with the scalar field on the sphere $s(\theta)$,

$$u(\beta) = \int d\Omega \, s(\theta)\psi(|\theta - \beta|). \tag{A2}$$

Expansion of these two scalar fields into spherical harmonics yields

$$s(\theta) = \sum_{\ell=0}^{\infty} \sum_{m=-\ell}^{+\ell} s_{\ell m} Y_\ell^m(\theta), \tag{A3}$$

$$\psi(\theta) = \sum_{\ell=0}^{\infty} \sum_{m=-\ell}^{+\ell} \psi_{\ell m} Y_\ell^m(\theta) = \sum_{\ell=0}^{\infty} \sqrt{\frac{2\ell+1}{4\pi}} \psi_{\ell 0} \, P_\ell(\cos\theta). \tag{A4}$$

The last step assumes central symmetry. In this case, only modes with $m = 0$ are contributing. For proceeding, the addition theorem for Legendre polynomials $P_\ell(x)$ (Arfken & Weber 1995) is used in substituting $\gamma = |\theta - \beta|$:

$$P_\ell(\cos\gamma) = \frac{4\pi}{2\ell+1} \sum_{m=-\ell}^{+\ell} Y_\ell^m(\theta) \, Y_\ell^{m*}(\beta). \tag{A5}$$

Combining these equations and applying the completeness relation yields the convolution relation for a centrally symmetric filter kernel,

$$u(\beta) = \sum_{\ell=0}^{\infty} \sum_{m=-\ell}^{+\ell} u_{\ell m} Y_\ell^m(\beta), \quad \text{with} \quad u_{\ell m} = \sqrt{\frac{4\pi}{2\ell+1}} s_{\ell m} \, \psi_{\ell 0}. \tag{A6}$$

A3 Concepts of optimized filtering on the sphere

The idea of optimized matched filters was proposed by Tegmark & de Oliveira-Costa (1998), and generalized to scale-adaptive filters by Sanz et al. (2001) for a flat topology. The construction of a centrally symmetric optimized filter function $\psi(\theta)$ for the amplification and detection of signal profiles differing only in size but not in shape implies a family of filters $\psi(\theta/R)$ introducing a scaling parameter R. Decomposing the family of filter functions $\psi(\theta/R)$ into spherical harmonics yields

$$\psi\left(\frac{\theta}{R}\right) = R^2 \sum_{\ell=0}^{\infty} \sqrt{\frac{2\ell+1}{4\pi}}\, \psi_{\ell 0}(R)\, P_\ell(\cos\theta), \tag{A7}$$

$$\psi_{\ell 0}(R) = \frac{1}{R^2} \int \mathrm{d}^2\theta \sqrt{\frac{2\ell+1}{4\pi}}\, \psi\left(\frac{\theta}{R}\right) P_\ell(\cos\theta), \tag{A8}$$

while allowing for central symmetry of the filter function. For a particular choice of R the filtered field $u(R, \boldsymbol{\beta})$ is obtained by convolution (cf. Section A2):

$$u(R, \boldsymbol{\beta}) = \sum_{\ell=0}^{\infty} \sum_{m=-\ell}^{+\ell} u_{\ell m} Y_\ell^m(\boldsymbol{\beta}) \quad \text{and} \tag{A9}$$

$$u_{\ell m} = \sqrt{\frac{4\pi}{2\ell+1}}\, s_{\ell m}\, \psi_{\ell 0}(R). \tag{A10}$$

Taking into account the vanishing expectation value of the noise $\langle n_v(\theta) \rangle = 0$, the expectation value of the filtered field at the North pole $\boldsymbol{\beta} = \mathbf{0}$ is given by

$$\langle u(R, \mathbf{0}) \rangle = A \sum_{\ell=0}^{\infty} \tau_{\ell 0}\, \psi_{\ell 0}(R). \tag{A11}$$

Assuming that the power spectrum of the signal is negligible compared to the noise power spectrum, the variance of the filtered field is given by

$$\sigma_u^2(R) = \langle [u(R, \boldsymbol{\beta}) - \langle u(R, \boldsymbol{\beta}) \rangle]^2 \rangle = \sum_{\ell=0}^{\infty} C_\ell\, \psi_{\ell 0}^2(R). \tag{A12}$$

While the optimized *matched filter* in the case of single frequency observations is defined to obey the first two of the following conditions, the optimized *scale-adaptive filter* is required to obey all three conditions given below.

(i) The filtered field $u(R, \mathbf{0})$ is an unbiased estimator of the source amplitude A at the true source position, i.e. $\langle u(R, \mathbf{0}) \rangle = A$.

(ii) The variance of $u(R, \boldsymbol{\beta})$ has a minimum at the scale R ensuring that the filtered field is an efficient estimator.

(iii) The expectation value of the filtered field at the source position has an extremum with respect to the scale R, implying

$$\frac{\partial}{\partial R} \langle u(R, \mathbf{0}) \rangle = 0. \tag{A13}$$

A4 Matched filter

In order to derive the matched filter, constraint (i) can be rewritten yielding

$$\sum_{\ell=0}^{\infty} \tau_{\ell 0}\, \psi_{\ell 0} = 1. \tag{A14}$$

Performing functional variation (with respect to the filter function ψ) of $\sigma_u^2(R)$ while incorporating the constraint (A14) through a Lagrangian multiplier yields the spherical matched filter:

$$\psi_{\ell 0} = \alpha\, \frac{\tau_{\ell 0}}{C_\ell}, \quad \text{where} \quad \alpha^{-1} = \sum_{\ell=0}^{\infty} \frac{\tau_{\ell 0}^2}{C_\ell}. \tag{A15}$$

In any realistic application, the power spectrum C_ℓ can be estimated from the observed data provided the power spectrum of the signal is negligible. The quantities α, $\tau_{\ell 0}$, and thus the filter kernel $\psi_{\ell 0}$ can be straightforwardly computed for any model source profile $\tau(\theta)$.

A5 Scale-adaptive filter

The next step consists of reformulating constraint (iii) in order to find a convenient representation for the application of functional variation. The expansion coefficient of the family of filter functions $\psi(\theta/R)$ of equation (A7) can be rewritten yielding

$$\psi_{\ell 0}(R) = \frac{1}{R^2} \int \mathrm{d}^2\theta\, \psi\left(\frac{\theta}{R}\right) Y_\ell^0(\theta) = \int \mathrm{d}^2\beta\, \psi(\beta) Y_\ell^0(R\beta), \tag{A16}$$

where $\beta \equiv \theta/R$. In general, this substitution is *not* valid, because $\mathrm{d}^2\theta = \sin\theta\, \mathrm{d}\theta\, \mathrm{d}\phi$. In the case of localized source profiles, the angle θ is small for non-vanishing values of ψ justifying the approximation $\sin\theta \approx \theta$. The same argument also applies for the boundaries of integration. With the aid of equation (A11), condition (A13) reads

$$\frac{\partial}{\partial R} \langle u(R, \mathbf{0}) \rangle = \sum_{\ell=0}^{\infty} \tau_{\ell 0}\, \frac{\partial \psi_{\ell 0}(R)}{\partial R} = 0. \tag{A17}$$

Using equation (A16), the derivative now acts on the Legendre polynomial P_ℓ,

$$\sum_{\ell=0}^{\infty} \sqrt{\frac{2\ell+1}{4\pi}}\, \tau_{\ell 0} \int \mathrm{d}^2\beta\, \psi(\beta) P_\ell'(\cos R\beta)\, \beta\, \sin R\beta = 0. \tag{A18}$$

Using the derivative relation of the Legendre polynomials (Arfken & Weber 1995),

$$P_\ell'(x) = \frac{\ell+1}{1-x^2}\, [x\, P_\ell(x) - P_{\ell+1}(x)], \tag{A19}$$

one obtains

$$\sum_{\ell=0}^{\infty} \sqrt{\frac{2\ell+1}{4\pi}}\, (\ell+1)\, \tau_{\ell 0} \int \mathrm{d}^2\beta\, \psi(\beta) \frac{R\beta}{\sin R\beta}$$
$$\times [\cos R\beta\, P_\ell(\cos R\beta) - P_{\ell+1}(\cos R\beta)] = 0. \tag{A20}$$

In our case, the angle θ is small for non-vanishing values of ψ justifying the approximations $\sin R\beta \approx R\beta$ and $\cos R\beta \approx 1$. Substituting back, $\mathrm{d}^2\beta = \mathrm{d}^2\theta/R^2$, introducing $x \equiv \cos\theta = \cos R\beta$, and inserting the inversion of equation (A16), namely

$$\psi(\beta) = \sum_{\ell'=0}^{\infty} \psi_{\ell'0}(R) Y_{\ell'0}^0(R\beta), \tag{A21}$$

one arrives at

$$\sum_{\ell',\ell=0}^{\infty} \sqrt{\frac{2\ell+1}{4\pi}} \sqrt{\frac{2\ell'+1}{4\pi}}\, (\ell+1)\, \tau_{\ell 0} \psi_{\ell'0}(R)$$
$$\times \frac{2\pi}{R^2} \int \mathrm{d}x\, P_{\ell'}(x)[P_\ell(x) - P_{\ell+1}(x)] = 0. \tag{A22}$$

Applying the orthogonality relation for the Legendre polynomials,

$$\int_{-1}^{+1} dx\ P_\ell(x) P_{\ell'}(x) = \frac{2}{2\ell+1} \delta_{\ell\ell'}, \tag{A23}$$

and using the small angle approximation in the second term of equation (A22) with the same argument as given above, yields the final result

$$\sum_{\ell=0}^{\infty} \psi_{\ell 0}(R)[\tau_{\ell 0} + \ell(\tau_{\ell 0} - \tau_{\ell-1,0})] = 0. \tag{A24}$$

Replacing the differential quotient with the corresponding derivative is a valid approximation for $\ell \gg 1$. Thus, equation (A24) can be recast in shorthand notation yielding

$$\sum_{\ell=0}^{\infty} \psi_{\ell 0}(R)\tau_{\ell 0} \left[2 + \frac{d \ln \tau_{\ell 0}}{d \ln \ell} \right] = 0. \tag{A25}$$

This result could have been obtained independently by attaching the tangential plane to the North pole and applying Fourier decomposition of the filter function ψ and the source profile τ. For that reason, it is not surprising that the functional form of this condition on the sphere agrees with that obtained by Sanz et al. (2001) for a flat topology in two dimensions.

Performing functional variation (with respect to the filter function ψ) of $\sigma_u^2(R)$ while interlacing the constraints (A14) and (A25) through a pair of Lagrangian multipliers yields the spherical scale-adaptive filter,

$$\psi_{\ell 0} = \frac{\tau_{\ell 0}}{C_\ell \Delta} \left[2b + c - (2a + b)\frac{d \ln \tau_{\ell 0}}{d \ln \ell} \right],$$
$$\Delta = ac - b^2, \tag{A26}$$

$$a = \sum_{\ell=0}^{\infty} \frac{\tau_{\ell 0}^2}{C_\ell}, \quad b = \sum_{\ell=0}^{\infty} \frac{\tau_{\ell 0}}{C_\ell} \frac{d\tau_{\ell 0}}{d\ell},$$

$$c = \sum_{\ell=0}^{\infty} C_\ell^{-1} \left(\frac{d\tau_{\ell 0}}{d \ln \ell} \right)^2. \tag{A27}$$

As before in the case of the matched filter, the power spectrum C_ℓ can be derived from observed data provided the power spectrum of the signal is negligible. Assuming a model source profile $\tau(\theta)$, the quantities $\tau_{\ell 0}, a, b, c$, and finally $\psi_{\ell 0}$ can be computed in a straightforward way. The derivative of $\tau_{\ell 0}$ with respect to the multipole order ℓ is a shorthand notation of the differential quotient in equation (A24).

This paper has been typeset from a TEX/LATEX file prepared by the author.